

Autophagic reliance promotes metabolic reprogramming in oncogenic KRAS-driven tumorigenesis

H. Helen Lin^a, Yiyin Chung^a, Chun-Ting Cheng^a, Ching Ouyang^b, Yong Fu^a, Ching-Ying Kuo^a, Kevin K. Chi^a, Maryam Sadeghi^a, Peiguo Chu^c, Hsing-Jien Kung^d, Chien-Feng Li^e, Kirsten H. Limesand^f and David K. Ann^{a,g}

^aDepartment of Diabetes and Metabolic Diseases Research, City of Hope, Duarte, CA, USA; ^bCenter for Informatics, City of Hope, Duarte, CA, USA; ^cShared Pathology Core, City of Hope, Duarte, CA, USA; ^dDepartment of Biochemistry and Molecular Medicine, UC Davis Comprehensive Cancer Center, Sacramento, CA, USA; ^eDepartment of Pathology, Chi-Mei Medical Center, Tainan, Taiwan; ^fDepartment of Nutritional Sciences, University of Arizona, Tucson, AZ, USA; ^gIrell & Manella Graduate School of Biological Sciences, Beckman Research Institute, City of Hope, Duarte, CA, USA

ABSTRACT

Defects in basal autophagy limit the nutrient supply from recycling of intracellular constituents. Despite our understanding of the prosurvival role of macroautophagy/autophagy, how nutrient deprivation, caused by compromised autophagy, affects oncogenic KRAS-driven tumor progression is poorly understood. Here, we demonstrate that conditional impairment of the autophagy gene *Atg5* (*atg5*-KO) extends the survival of KRAS^{G12V}-driven tumor-bearing mice by 38%. *atg5*-KO tumors spread more slowly during late tumorigenesis, despite a faster onset. *atg5*-KO tumor cells displayed reduced mitochondrial function and increased mitochondrial fragmentation. Metabolite profiles indicated a deficiency in the nonessential amino acid asparagine despite a compensatory overexpression of ASNS (asparagine synthetase), key enzyme for *de novo* asparagine synthesis. Inhibition of either autophagy or ASNS reduced KRAS^{G12V}-driven tumor cell proliferation, migration, and invasion, which was rescued by asparagine supplementation or knockdown of MFF (mitochondrial fission factor). Finally, these observations were reflected in human cancer-derived data, linking ASNS overexpression with poor clinical outcome in multiple cancers. Together, our data document a widespread yet specific asparagine homeostasis control by autophagy and ASNS, highlighting the previously unrecognized role of autophagy in suppressing the metabolic barriers of low asparagine and excessive mitochondrial fragmentation to permit malignant KRAS-driven tumor progression.

Abbreviations: ACTA1: actin, alpha 1; AHR: aryl-hydrocarbon receptor; ASNS: asparagine synthetase; ATF4: activating transcription factor 4; ATG5: autophagy-related 5; ATG7: autophagy-related 7; COX4I1: cytochrome c oxidase subunit 4I1; DCF: dichlorofluorescein; DiOC6: 3,3'-dihexyloxacarbocyanine iodide; DMFS: distal metastasis-free survival; DNM1L: dynamin 1-like; ECAR: extracellular acidification rate; EMT: epithelial-to-mesenchymal transition; ERBB2/HER2: erb-b2 receptor tyrosine kinase 2; HRAS: harvey rat sarcoma virus oncogene; IL6: interleukin 6; KD: knockdown; KO: knockout; KRAS: kirsten rat sarcoma viral oncogene homolog; MAP1LC3B/LC3B: microtubule-associated protein 1 light chain 3 beta; MAPK: mitogen-activated protein kinase; MFF: mitochondrial fission factor; MKI67: antigen identified by monoclonal antibody Ki 67; NAC: N-acetyl-L-cysteine; NCBI-GEO: National Center for Biotechnology Information-Gene Expression Omnibus; NKI: Netherlands Cancer Institute; OCR: oxygen consumption rate; PI: propidium iodide; PyMT: polyoma middle T antigen; RB1CC1/FIP200: RB1 inducible coiled-coil 1; ROS: reactive oxygen species; SDC: salivary duct carcinoma; SNAI1/SNAI1: snail family zinc finger 1; SNAI2/SLUG: snail family zinc finger 2; SQSTM1/p62: sequestosome 1; TGFB1: transforming growth factor, beta 1; TNBC: triple negative breast cancer; WT: wild type

ARTICLE HISTORY

Received 21 June 2017
Revised 28 February 2018
Accepted 6 March 2018



KEYWORDS



Asparagine; asparagine synthetase; autophagy; MFF; metabolic reprogramming; mitochondria; oncogenic KRAS

Introduction

Oncogenic RAS mutations are found in approximately 30% of cancers, and lead to poor prognosis. The RAS type GTPase family oncoproteins (HRAS, NRAS, and KRAS) are considered “undruggable,” causing a shortage of therapeutic options. Therefore, a potential treatment approach for RAS-associated cancers is to target their metabolic vulnerabilities. One such metabolic vulnerability is that many KRAS-driven tumors become dependent on autophagy for survival [1]. Autophagy is

a normal catabolic process, which safeguards quality control in organelles by removing and recycling protein aggregates to maintain cell and tissue homeostasis. However, there is no consensus on the role of autophagy in cancer. For instance, in RAS-induced pancreatic tumors, disruption of macroautophagy/autophagy, by knockout of the essential autophagy related genes *Atg5* or *Atg7*, accelerates the emergence of pre-malignant lesions [2,3]. By contrast, in PyMT oncogene-driven mammary tumors, disruption of autophagy by *Rb1cc1/Fip200* (RB1-

CONTACT David K. Ann  dann@coh.org  Beckman Research Institute, City of Hope Cancer Center, Duarte, CA 91010-3000

 Supplemental data for this article can be accessed at:  <https://doi.org/10.1080/15548627.2018.1450708>

inducible coiled-coil 1) ablation, suppresses tumorigenesis [4]. Furthermore, a recent study shows that autophagy is dispensable for KRAS-driven tumor cell proliferation in vitro or tumorigenesis in vivo, in a xenograft study [5]. Therefore, the role of autophagy in cancer is complex, and likely depends on the context, type, and stage of tumors.

Given the complex role of autophagy, it is debatable whether there is a unifying molecular mechanism to resolve the role of autophagy in cancer progression. Various mechanistic pathways have been proposed for both the pro- and anti-cancer functions of autophagy. For instance, autophagy is required for anti-cancer immunosurveillance, which prevents tumorigenesis [6]. In contrast, autophagy promotes tumorigenesis by recycling proteins, thereby meeting the high metabolic demands of rapidly dividing cancer cells [7,8]. Other pro-tumorigenic consequences of autophagy include promoting the secretion of pro-invasive cytokines, such as TGF β 1 (transforming growth factor, beta 1), and inducing the epithelial-to-mesenchymal transition (EMT) [8]. Recent reports have shown that AHR (aryl-hydrocarbon receptor) negatively regulates autophagy and EMT in lung cancer [9], whereas the E3 ubiquitin ligase MARCH5 (membrane-associated ring finger [C3HC4] 5) promotes autophagy, migration and invasion in ovarian cancer cells [10]. One plausible explanation is that autophagy modulates several targets, which act in mutual opposition to regulate tumor initiation, progression, and invasion. Thus, autophagy inhibition could result in different outcomes depending on the timing, duration, or method of inhibition during tumorigenesis. Further insight into the mechanisms linking autophagy and cancer is required to clarify elements that influence cancer progression.

The objective of this study was to identify the molecular mechanisms underlying the intricate connection of autophagy with cancer. Accordingly, we examined the impact of autophagy loss in a well-characterized salivary duct carcinoma (SDC) mouse model driven by oncogenic KRAS^{G12V} combined with *Atg5* knockout (*atg5*-KO). These highly aggressive tumors show similarity to ductal carcinoma of the breast and may serve as a model for tumors of ductal origin. We found that blocking autophagy promotes early tumorigenesis but slows tumor growth, leading to extended survival, and indicating that the timing of autophagy disruption is important for its effects. Using this model, we characterized the autophagic regulation of oncogenic KRAS-driven metabolic reprogramming. By studying the intracellular level of asparagine, a nonessential amino acid, and mitochondrial integrity in *atg5*-KO tumor cells, we found that autophagy is essential for oncogenic KRAS to reprogram and rewire cellular metabolism, especially mitochondrial function and amino acid profiling. Of note, low asparagine or excessive mitochondrial fission decreased KRAS^{G12V}-driven tumor cell motility and invasion. The mechanistic link between impaired autophagy with attenuated cell migration was validated by the supplementation of asparagine or knockdown of MFF (mitochondrial fission factor). The critical tumor-promoting role of asparagine is further supported by the overexpression of ASNS (asparagine synthetase), key enzyme for *de novo* asparagine biosynthesis, is associated with poor clinical outcomes in multiple human cancers. Collectively, our findings show that autophagy has a dual role in

experimental KRAS-mediated tumorigenesis, with an overall pro-cancer effect. Furthermore, a pathway connecting autophagy, asparagine, and mitochondrial integrity is critical for oncogenic KRAS-transformed tumor cell migration and invasion, providing mechanistic insights into the role of autophagy in tumor progression.

Results

Autophagy deficiency extends survival in an experimental KRAS^{G12V} tumor model

Earlier studies established a mouse tumor model with inducible salivary ductal cell-specific activation of oncogenic KRAS^{G12V} to recapitulate the local invasion and sarcomatoid manifestation of human SDC [11]. To test the role of autophagy in the various stages of SDC development, we crossed the KRAS^{G12V} SDC mice [11] with a mouse model for conditional genetic disruption of the essential autophagy protein ATG5 (*Atg5^{fllox/fllox}*) [12,13]. ATG5 is required for the formation of autophagosomes [12,14]. The simultaneous *Ela-CreERT*-dependent induction of KRAS^{G12V} and ablation of *Atg5* in the salivary ductal cells of KRAS^{G12V};*atg5* ^{Δ/Δ} mice was achieved through tamoxifen-inducible Cre-Lox recombination. Deletion of *Atg5* did not block the formation of SDC in KRAS^{G12V};*atg5* ^{Δ/Δ} animals. Immunohistochemistry (IHC) analysis revealed low levels of both ATG5 and MAP1LC3B/LC3B (microtubule-associated protein 1 light chain 3 beta) (Figure 1A), and western analyses showed low ATG5, moderately elevated SQSTM1/p62 (sequestosome 1) levels, and a higher LC3B-I:II ratio indicating that autophagy was impaired in SDC of KRAS^{G12V};*atg5* ^{Δ/Δ} mice (Figure 1B). At d 24 after administration of tamoxifen, the average weight of KRAS^{G12V};*Atg5* ^{$+/+$} tumor-bearing submandibular glands was significantly higher than that of the KRAS^{G12V};*atg5* ^{Δ/Δ} tumor-bearing glands (Figure 1C). Accordingly, d 24 tumors from KRAS^{G12V};*atg5* ^{Δ/Δ} mice often exhibited areas of normal tissue admixed with tumor tissues, whereas the KRAS^{G12V};*Atg5* ^{$+/+$} tumors had fewer normal tissue regions (Figure S1A-D). Furthermore, although the KRAS^{G12V};*atg5* ^{Δ/Δ} tumors were often confined within the submandibular glands, the KRAS^{G12V};*Atg5* ^{$+/+$} tumors diffusely infiltrated the interlobular and peri-salivary gland soft tissue (Figure 1D, S1E and S1F). The growth rate of primary tumor cells from the KRAS^{G12V};*Atg5* ^{$+/+$} mice was significantly higher than that from the KRAS^{G12V};*atg5* ^{Δ/Δ} mice (Figure 1E). Lastly, Kaplan-Meier survival curves showed that genetic disruption of *Atg5* in the KRAS^{G12V}-driven SDC mouse model extended the post-induction median survival by 38%, compared with KRAS^{G12V};*Atg5* ^{$+/+$} mice (Figure 1F, $p = 0.0045$). In summary, ablation of *Atg5* did not block the formation of KRAS^{G12V}-driven SDC tumors, but loss of autophagy reduced the tumor burden and prolonged survival.

Nonequivalent roles of autophagy during oncogenic KRAS-driven tumor initiation and tumor progression

To gain insight into the complex role of autophagy during tumor development, we performed histological analysis of submandibular glands at multiple time points, generally from d 9

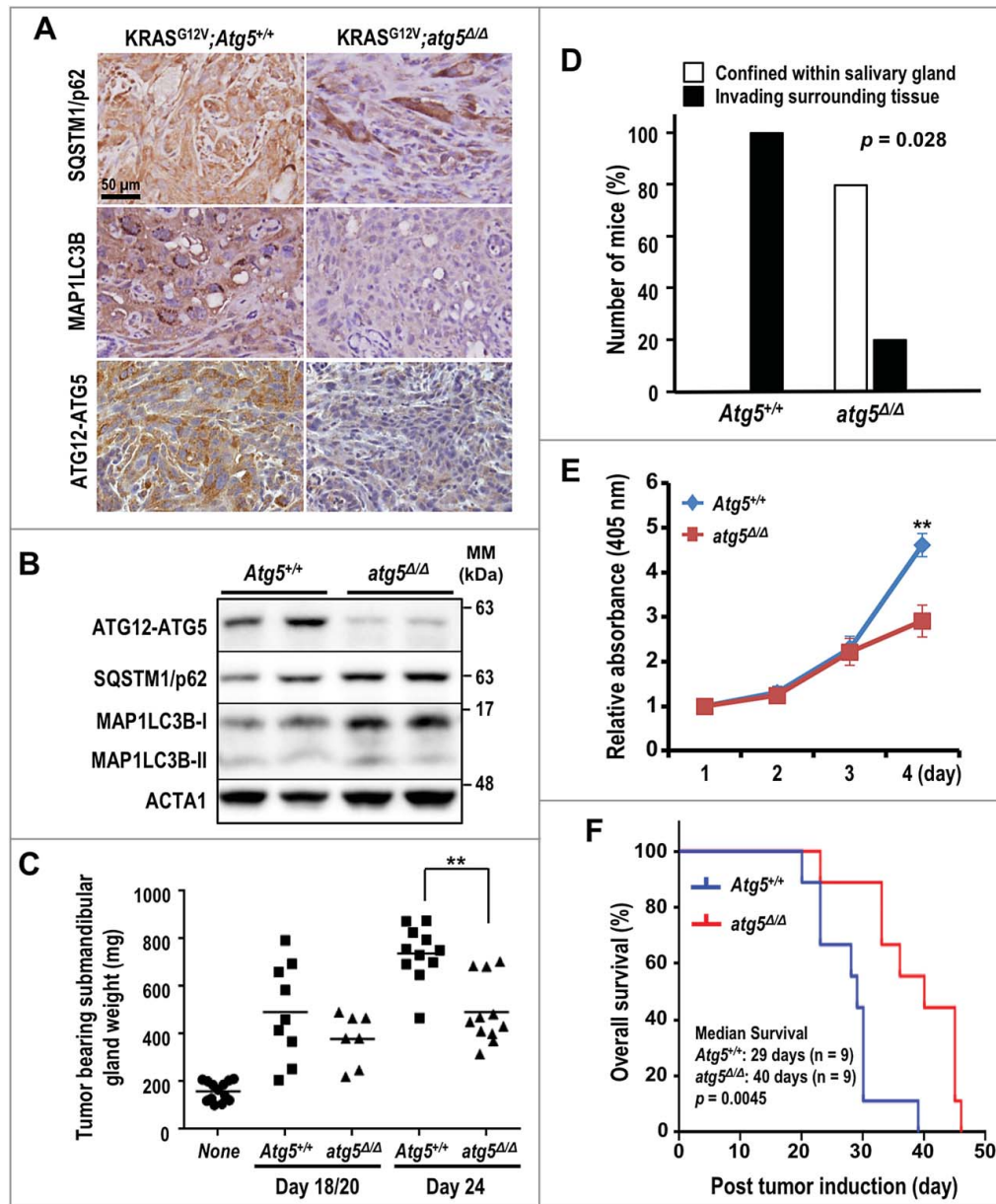


Figure 1. Enhanced survival of autophagy-deficient *KRAS^{G12V};atg5^{Δ/Δ}* mice. (A) Representative IHC of SQSTM1, LC3B and ATG12–ATG5 in SDC tumors from *KRAS^{G12V};Atg5^{+/+}* and *KRAS^{G12V};atg5^{Δ/Δ}* mice (d 15). The SDC tumors from *KRAS^{G12V};atg5^{Δ/Δ}* mice (d 15) show the loss of ATG12–ATG5 and LC3B staining in tumor cells. Scale bar: 50 μ m. (B) Western analyses of lysate of SDC tumors recovered from *KRAS^{G12V};Atg5^{+/+}* and *KRAS^{G12V};atg5^{Δ/Δ}* mice with the indicated antibodies. (C) Increased tumor burden in *KRAS^{G12V};Atg5^{+/+}* mice. Submandibular glands from *KRAS^{G12V};Atg5^{+/+}* and *KRAS^{G12V};atg5^{Δ/Δ}* mice were harvested at d 18 and 20 (d 18/20 combined group), and d 24 post-tamoxifen and wet weights were recorded. Submandibular glands from untreated littermates serve as controls and are designated as "none". $p = 0.0045$ between *KRAS^{G12V};Atg5^{+/+}* and *KRAS^{G12V};atg5^{Δ/Δ}* cohorts at d 24 ($n \geq 7$). (D) Extra-salivary-gland invasion in the *KRAS^{G12V};Atg5^{+/+}* cohort at d 20 ($p = 0.028$, $n = 5$). (E) Autophagy promotes cell growth in vitro. In vitro cell growth analysis was performed by seeding *KRAS^{G12V};Atg5^{+/+}* and *KRAS^{G12V};atg5^{Δ/Δ}* primary tumor cells at low density and measuring viability every 24 h for 4 consecutive d by ACP analysis. $**$: $p < 0.01$. (F) The Kaplan-Meier survival curves for *KRAS^{G12V};Atg5^{+/+}* and *KRAS^{G12V};atg5^{Δ/Δ}* mice after tumor induction by tamoxifen ($n = 9$ for each cohort). $p = 0.0045$ (log-rank test).

to d 20 at 3-d intervals post tamoxifen treatments. Humane endpoints were typically reached in tumor-bearing mice d 20 after tumor induction, and euthanasia ensued. Similar to staging of human salivary gland cancers (<https://www.cancer.org/cancer/salivary-gland-cancer/detection-diagnosis-staging/staging.html>), time points were chosen based on the size of the tumor. We observed more hyperplastic tumor foci in the *KRAS^{G12V};atg5^{Δ/Δ}* mice, as early as at 9 d after tumor induction, compared with *KRAS^{G12V};Atg5^{+/+}* mice (Figure 2A and 2B). By d 12, we observed high variability in the mean tumor burden (tumor-to-gland area ratio) with a trend toward an increase in

the *KRAS^{G12V};atg5^{Δ/Δ}* mice; however, tumor burden in *KRAS^{G12V};Atg5^{+/+}* mice caught up at later time points (Figure 2C and 2D). To reconcile the increased tumor focus formation with the increased overall survival of the *KRAS^{G12V};atg5^{Δ/Δ}* mice, we measured proliferation using antibodies for phospho-Histone H3 (Ser10), which labels cells in the mitotic (M) phase, and MKI67/Ki-67, which labels proliferative cells. In contrast to the increased tumor initiation, there were fewer M-phase and proliferating cells in the *Atg5*-deficient mice at d 15 to 20 after tamoxifen administration, compared with the autophagy-competent controls (Figure 2E–H and S2).

Furthermore, the number of phospho-H3(Ser10)-positive proliferating cells in tumors of the SDC-*Atg5*^{+/+} mice increased from d 9 to d 18, and was sustained until d 20 (Figure 2F). Also, the number of proliferating cells was consistently higher in *KRAS*^{G12V};*Atg5*^{+/+} tumors than in tumors of *KRAS*^{G12V};*atg5*^{Δ/Δ} littermates at d 15 through d 20 time points (Figure 2H). Lastly, tumors from *KRAS*^{G12V};*Atg5*^{+/+} mice invaded the interlobular septal stroma (Figure S3), which was

rare in tumors from *KRAS*^{G12V};*atg5*^{Δ/Δ} littermates. Therefore, although the loss of ATG5-regulated autophagy accelerated oncogenic transformation at the onset of *KRAS*^{G12V} activation, as evidenced by an initial increase in tumor foci, loss of autophagy also blocked progression of the tumor foci to sarcomatoid tumors. This reduced rate of progression may account for the survival advantage of *KRAS*^{G12V};*atg5*^{Δ/Δ} tumor-bearing mice (Figure 1F).

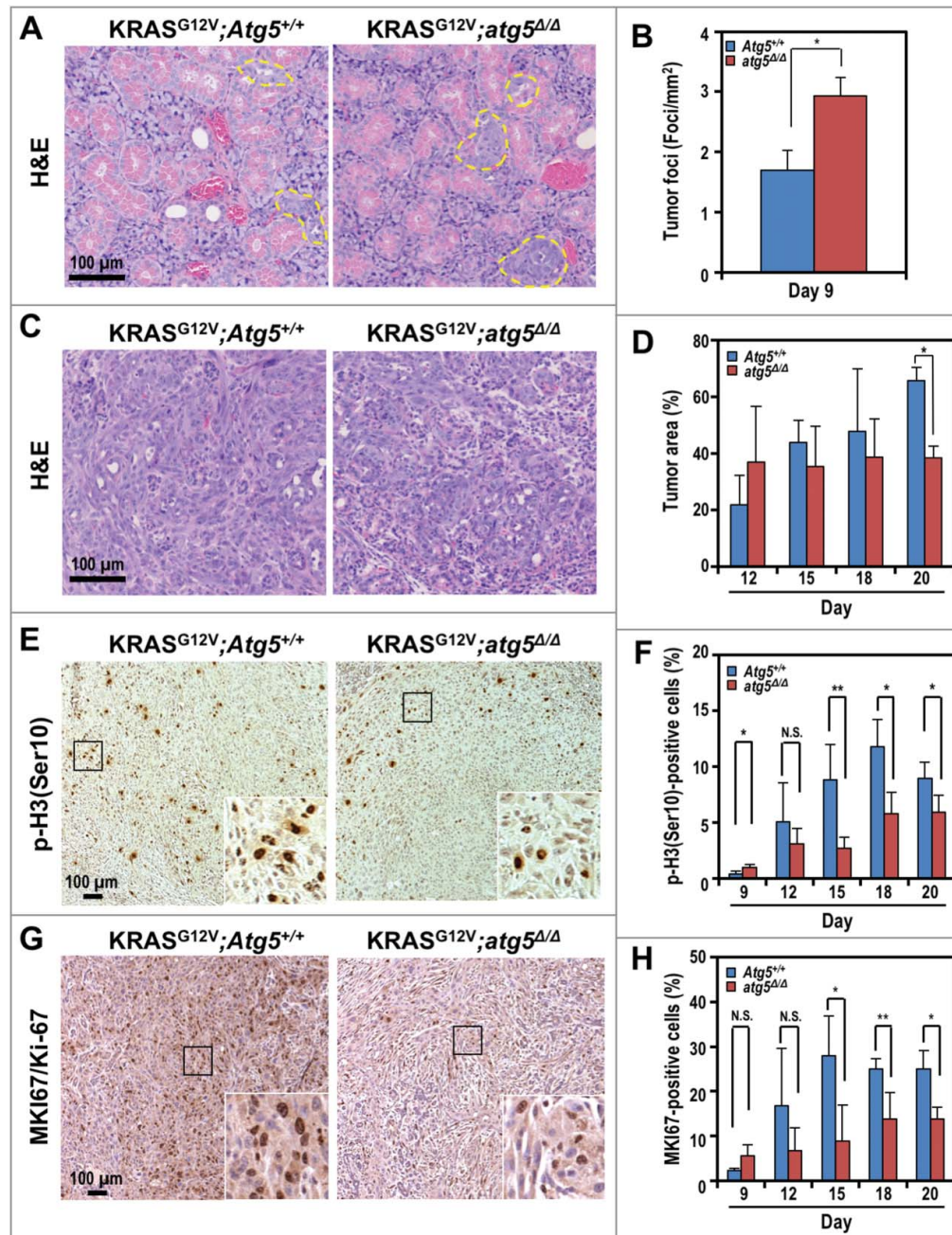


Figure 2. Accelerated tumor initiation and delayed progression of SDCs in *KRAS*^{G12V};*atg5*^{Δ/Δ} mice. (A) Representative histological analyses (hematoxylin and eosin, or H&E staining) of submandibular glands at d 9 post tumor induction. Yellow dotted line: tumor foci. (B) Quantification of tumor foci number on d 9. (C) Representative histological analyses (H&E staining) of submandibular glands at d 12 post tumor induction. At d 12, the *Atg5*^{+/+} mice showed diffuse spindle tumor cells infiltrating the peri-acinar tissue, while in the *atg5*^{Δ/Δ} mice, the tumor cells formed nodules with less microinvasion. (D) Quantification of percentage of tumor area on d 12, 15, 18 and 20. (E and G) Representative IHC of proliferation markers, phospho-histone H3 (Ser10) (p-H3(Ser10); E) and MKI67 (G) in d 20 SDCs from *KRAS*^{G12V};*Atg5*^{+/+} and *KRAS*^{G12V};*atg5*^{Δ/Δ} mice. Expanded view of the boxed area was shown on bottom right corner of each image. (F and H) Quantification of p-H3(Ser10) (F) and MKI67/Ki-67 (H) stained cells relative to the total cell number at d 9, 12, 15, 18, and 20. Representative IHCs shown in Figure S2. Three random low-power fields were quantified from each mouse. Data are shown as mean ± S.D.; n ≥ 4. *: p < 0.05; **: p < 0.01; N.S.: not significant (Student t test, 2-tailed, unpaired). Scale bar: 100 μm.

Autophagy disruption impairs mitochondrial bioenergetics in tumor cells

Multiple primary tumor cells were isolated from both genotypes to perform molecular analyses. The ex vivo morphology was similar between primary *atg5*-KO and *Atg5*-WT tumor cells and autophagy deficiency in *atg5*-KO cells is supported by western analyses showing reduced ATG5, elevation in SQSTM1 level, and reduced LC3B-I to LC3B-II conversion (Figure S4A-D). Next, we determined whether loss of autophagy impairs oncogenic KRAS-mediated metabolic reprogramming by systematically comparing the molecular circuitry governing the bioenergetic state ex vivo. Compromised autophagy reduced the basal respiration and diminished the spare respiratory capacity, as measured by the oxygen consumption rate (OCR) assay (Figure 3A), suggesting that ATG5 loss impairs oxidative metabolism and reduces mitochondrial function. However, the rate of glycolysis and glycolytic capacity, reflected by the extracellular acidification rate (ECAR), were similar between tumor cells from both genotypes (Figure 3B). As expected, reduced oxidative respiration, without a compensatory increase in glycolytic rate, lowered ATP production (Figure 3C). These results are consistent with a model wherein the reduced cell proliferation rate (Figure 1E) and suppressed OCR and ATP production (Figure 3A and 3C) reduce the tumor burden, and extend the survival of autophagy-impaired SDC tumor-bearing mice (Figure 1F).

Consistent with reduced OCR, the reactive oxygen species (ROS) level, measured as the fluorescence intensity of oxidized dichlorofluorescein (DCF), was lower in *atg5*-KO tumor cells, (Figure 3D and 3E). Although treatment with the ROS scavenger N-acetyl-L-cysteine (NAC, 5 mM) reduced the oxidized DCF levels in *Atg5*-WT cells, NAC (even at 10 mM) was marginally effective in suppressing ROS production in *atg5*-KO tumor cells (Figure 3F). To determine the role of autophagy in regulating mitochondrial dynamics, we used fluorescence imaging to examine the morphological features of cellular mitochondria in isolated tumor cells tagged with the DsRed-labeled mitochondrial matrix marker COX4I1 (cytochrome c oxidase subunit 4I1). In agreement with the reduced OCR and ROS production observed in isolated *atg5*-KO tumor cells, more over-fragmented mitochondria with smaller networks were noted (Figure 3G), compared with the *Atg5*-WT tumor cells (Figure 3H). This finding was further corroborated by the observation of a lower mitochondrial membrane potential, as measured by 3,3'-dihexyloxycarbocyanine iodide (DiOC6) fluorescence, in $KRAS^{G12V};atg5^{\Delta/\Delta}$ tumor cells (Figure 3I). Together, we conclude that the excessive mitochondrial fragmentation may account for attenuated mitochondrial output in $KRAS^{G12V};atg5^{\Delta/\Delta}$ tumor cells.

Autophagy disruption impairs mitochondrial dynamics in tumor cells

Mitochondrial architecture is crucial for cell viability, proliferation, senescence, and signaling. Because overexpression of MFF and/or DNMI1 (dynamain 1-like) promotes mitochondrial fission and fragmentation [15,16], which is likely exacerbated by compromised autophagy, we examined the expressions of selected mitochondrial fission and electron transport complex

proteins in tumors from both $KRAS^{G12V};Atg5^{+/+}$ and $KRAS^{G12V};atg5^{\Delta/\Delta}$ mice and compared with non-tumorous tissues. Notably, proteins from mitochondrial complexes II and V, as well as DNMI1, were higher in *atg5*-KO tumors than from *Atg5*-WT tumors (Figure 4A). Gene silencing of oncogenic *Kras* by *siKras* was performed to validate the effect of KRAS on increased DNMI1 and MFF protein levels in cultured tumor cells. As shown in Figure 4B, knockdown of KRAS decreased DNMI1 and MFF protein levels in *atg5*-KO tumor cells exclusively despite efficient knockdown of KRAS in *Atg5*-WT cells. It is possible that autophagy and oncogenic KRAS are redundant in regulating DNMI1 and MFF abundance. We then hypothesized that decreasing the drive toward fission would revert the mitochondrial fragmentation phenotype of the *atg5*-KO tumor cells, to mimic the elongated mitochondria observed in *Atg5*-WT tumor cells. To test this hypothesis, we transduced both *Atg5*-WT and *atg5*-KO tumor cells, respectively, with lenti-*shCtrl* or *-shMff* (Figure 4C and 4D). In primary *shCtrl* cells tagged with COX4I1-DsRed, the $KRAS^{G12V};atg5^{\Delta/\Delta}$ mitochondria were shorter and smaller than $KRAS^{G12V};Atg5^{+/+}$ mitochondria (Figure 4C and 4D). However, after silencing of *Mff* by *shMff*, the mitochondria were elongated and tubular-like, indicating decreased mitochondrial fission in the *atg5*-KO, but not the *Atg5*-WT tumor cells (Figure 4C). Even though fragmented mitochondria phenotype was partially reversed by silencing *Mff* in the $KRAS^{G12V};atg5^{\Delta/\Delta}$ cells, there were increases in both basal and ATP-linked respiration in *shMff* transduced cells when OCRs were measured (Figure 4E). Consistently, a significant increase in ATP production was detected in MFF-knockdown cells of both genotypes (Figure 4F).

Next, we confirmed the differential sensitivity of $KRAS^{G12V};Atg5^{+/+}$ and $KRAS^{G12V};atg5^{\Delta/\Delta}$ cells to the metabolic stress of nutrient starvation. As expected, *atg5*-KO cells exhibited greater sensitivity to deprivation of both glucose (Figure S5A, upper panel) and glutamine (Figure S5A, lower panel) than *Atg5*-WT cells. However, autophagy deficiency did not correlate with level of senescence markers CDKN2A/p16 (cyclin-dependent kinase inhibitor 2A) and CDKN1A/p21 (cyclin-dependent kinase inhibitor 1A), nor did it affect SNAI1/SNAI1 (snail family zinc finger 1) and/or SNAI2/SLUG (snail family zinc finger 2) transcription factors in both control and serum starvation conditions (Figure S5B). Likewise, autophagy deficiency also did not affect the populations of necrotic and apoptotic cells, as measured by flow cytometry using ANXA5/annexin V (annexin A5) and propidium iodide (PI) (Figure S5C and S5D). Altogether, our data suggest that impaired autophagy dysregulates mitochondrial dynamics and promotes the accumulation of over-fragmented and malfunctioning mitochondria. These results, combined with the reduced OCR observed in $KRAS^{G12V};atg5^{\Delta/\Delta}$ cells (Figure 3A), support a model wherein autophagy is critical for accelerated tumor progression when tumor cells encounter metabolic stress, under circumstances when nutrient demands exceed the local supply.

Autophagy differentially regulates oncogenic KRAS-rewired cellular metabolism

Oncogenic KRAS can reprogram glucose and glutamine metabolism [17,18], whilst autophagy is a critical regulator of cellular

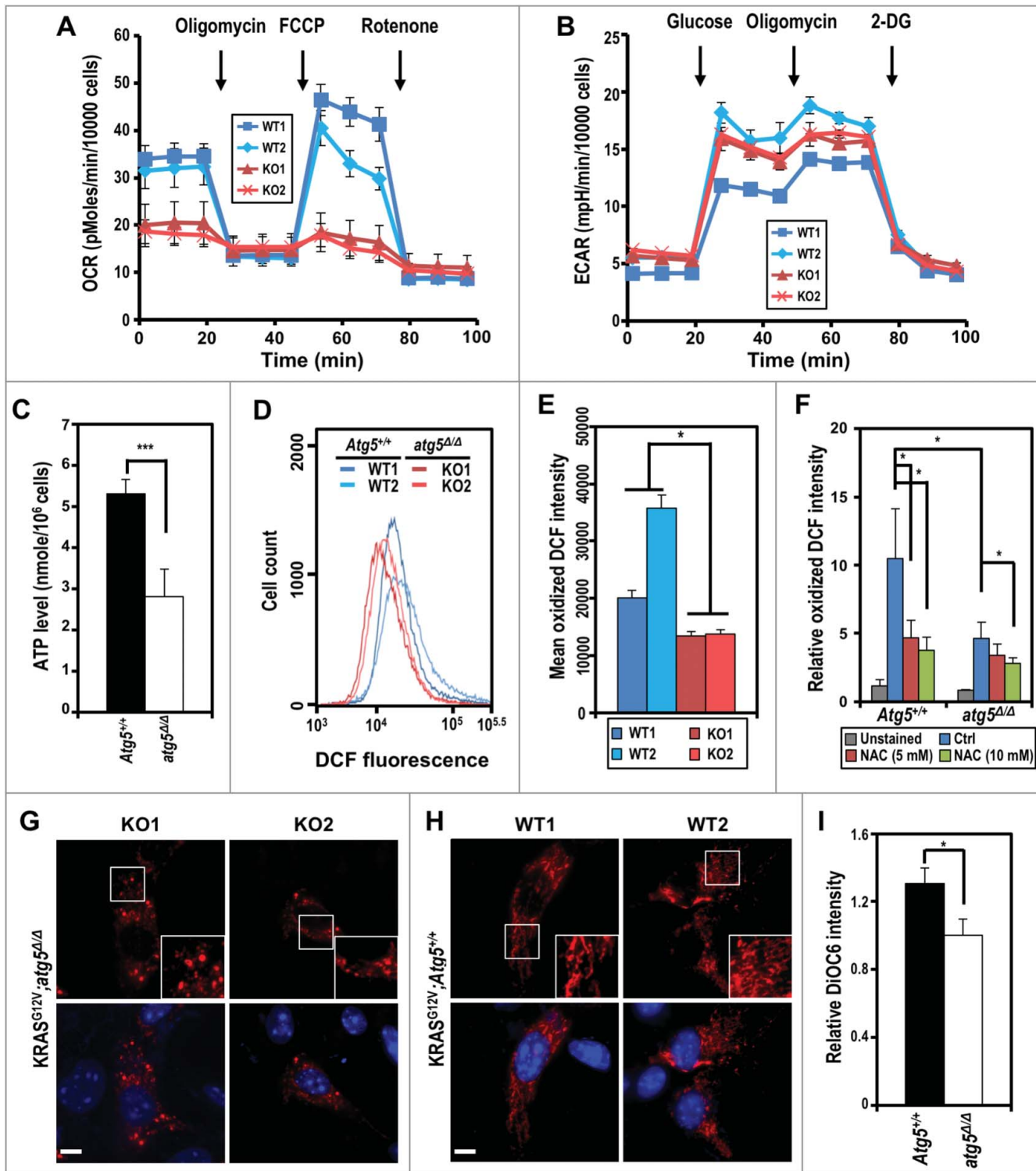


Figure 3. $\text{KRAS}^{\text{G12V}};$ $\text{atg5}^{\Delta/\Delta}$ tumor cells exhibit a lower oxygen consumption rate. (A and B) Oxygen consumption rate (OCR) (A) and extracellular acidification rate (ECAR) (B) were measured in $\text{KRAS}^{\text{G12V}};$ $\text{Atg5}^{+/+}$ (WT1, WT2; colored blue) and $\text{KRAS}^{\text{G12V}};$ $\text{atg5}^{\Delta/\Delta}$ (KO1, KO2; colored red) cells isolated from 2 individual mice of each genotype. Data are shown as the mean \pm S.D.; $n = 3$. (C) Levels of ATP were measured in $\text{KRAS}^{\text{G12V}};$ $\text{Atg5}^{+/+}$ and $\text{KRAS}^{\text{G12V}};$ $\text{atg5}^{\Delta/\Delta}$ cells. The ATP levels were normalized to cell number. Data are shown as mean \pm S.D.; $n = 3$. (D) Decreased intracellular reactive oxygen species (ROS) levels in $\text{KRAS}^{\text{G12V}};$ $\text{atg5}^{\Delta/\Delta}$ cells were measured by staining for oxidized dichlorofluorescein (DCF) and analyzed by flow cytometry. A representative flow cytometry plot of the DCF fluorescence intensity is shown. (E) Quantification of oxidized DCF fluorescent intensity. The intensity of DCF, oxidized from nonfluorescent DCFDA, was analyzed by flow cytometry. Relative oxidized DCF levels are calculated from mean DCF intensity of 2 independently isolated $\text{KRAS}^{\text{G12V}};$ $\text{Atg5}^{+/+}$ or $\text{KRAS}^{\text{G12V}};$ $\text{atg5}^{\Delta/\Delta}$ cells, respectively. Data are shown as the mean \pm S.D.; $n = 3$. (F) ROS levels in $\text{KRAS}^{\text{G12V}};$ $\text{Atg5}^{+/+}$ and $\text{KRAS}^{\text{G12V}};$ $\text{atg5}^{\Delta/\Delta}$ cells treated with N-acetyl cysteine (NAC), a ROS scavenger. SDC primary cells were treated with the indicated concentrations of NAC for 24 h prior to ROS detection by DCFDA staining. Relative oxidized DCF intensity was calculated by normalizing to unstained controls (set as 1). Data are shown as mean \pm S.D.; $n = 3$. (G and H) Autophagy-compromised $\text{KRAS}^{\text{G12V}};$ $\text{atg5}^{\Delta/\Delta}$ cells exhibit excessive fragmentation of the mitochondria. $\text{KRAS}^{\text{G12V}};$ $\text{atg5}^{\Delta/\Delta}$ (G) and $\text{KRAS}^{\text{G12V}};$ $\text{Atg5}^{+/+}$ (H) primary tumor cells were infected with lentiviral particles that express COX4I1-DsRed for visualizing mitochondria. The cells were seeded on collagen I-coated coverslips and fixed with 4% paraformaldehyde for imaging. SDC tumor cells from 2 mice of each genotypes were examined. Zoomed view of the boxed area was shown on the right bottom of each image. Scale bar: $10 \mu\text{m}$. (I) Autophagy-compromised $\text{KRAS}^{\text{G12V}};$ $\text{atg5}^{\Delta/\Delta}$ cells exhibit decreased mitochondrial membrane potential. Mitochondrial membrane potential was measured by 3,3'-dihydroxyl-oxa-carbocyanine iodide (DiOC6) staining and analyzed by flow cytometry. Relative DiOC6 intensity was calculated by setting the mean DiOC6 fluorescence intensity of $\text{KRAS}^{\text{G12V}};$ $\text{atg5}^{\Delta/\Delta}$ cells as 1. Data are shown as mean \pm S.D.; $n = 3$. *: $p < 0.05$; ***: $p < 0.001$ (Student *t* test, 2-tailed, unpaired).

metabolism and intracellular nutrient homeostasis [19]. To address the global impact of impaired autophagy on cellular metabolism in *atg5*-KO tumor cells, we performed a quantitative metabolomic comparison between tumor cells derived from *Atg5*-WT and *atg5*-KO tumors. We identified 9966 features from negative mode liquid chromatography–mass spectrometry analysis and top 4000 features with statistical significance were shown in Fig 5A. Both Heatmap and Metabolic impact analyses segregated the samples by compound, tightly grouping the replicates (Figure 5A, B). Among them, 92 differentially expressed metabolites were selected and subjected to pathway analysis based on KEGG pathway maps (Release 82.1) [20]. The analyses of metabolic impact and pathway enrichment showed that amino acids, pyrimidine and purine metabolism, and citrate cycle were the most affected metabolic pathways by compromised autophagy (Figure 5C; false discovery rate < 0.05). Of note, the finding that citric acid cycle metabolites are one of the most altered metabolic pathways is consistent with our mitochondrial functional assays (Figure 3A). As many amino acid metabolic pathways were significantly altered (Figure 5B), we quantified intracellular amino acids and found a decrease in the concentrations of 12 amino acids, including essential and nonessential amino acids, in autophagy-deficient tumor cells (Table 1; Figure S6A). In contrast, there was a significant increase in intracellular glutamine (Table 1; Figure S6A), but not glucose level (Figure S6B) in *atg5*-KO tumor cells. We next tested whether a specific amino acid insufficiency, resulting from impaired autophagy, is associated with reduced cell proliferation (Figure 1E).

Among all amino acids that were significantly decreased in *atg5*-KO tumor cells, aspartate and asparagine, 2 nonessential amino acids, caught our attention. This is because asparagine is synthesized *de novo* from aspartate by ASNS, whose upregulation is associated with the proliferation, migration, and tumorigenicity of cancer cells [21]. Although asparagine supplementation enhanced tumor cell proliferation independent of autophagy competency (Figure S6C, left panel), the effects on *atg5*-KO tumor cells appeared to be more pronounced (Figure S6C, right panel). To further consolidate the role of asparagine in growth of autophagy-deficient tumor cells, we examined the expression of asparagine-producing enzyme ASNS under metabolic stress. ASNS gain of function was confirmed by subjecting cells to glutamine deprivation (from 5 mM in control full medium to 0.5 mM), which is a major metabolic stress (Figure S6D, left panel). Notably, the abundance of *Asns* mRNA (in full medium) was higher in *atg5*-KO cells than in *Atg5*-WT cells (Figure S6D), suggesting an autophagy deficiency-upregulated *Asns* expression, perhaps through a compensatory mechanism, in response to asparagine deficiency. Indeed, supplementation with asparagine reduced the *Asns* mRNA level only in *atg5*-KO tumor cells, close to the level seen in *Atg5*-WT tumor cells (Figure S6D, right panel). Importantly, these findings suggest a link between autophagy and oncogenic KRAS-driven metabolic reprogramming.

Asparagine promotes cell motility in *atg5*-KO tumor cells

Cell motility is a high energy-demanding process. Since *shMff* boosted ATP production in SDC cells (Figure 4F), we

compared motility between *shMff*- and *shCtrl*-transduced *Atg5*-WT and *atg5*-KO tumor cells by scratch assay and found reduced motility, which was reversed by *Mff*-silencing in *atg5*-KO tumor cells (Figure S7A). Based on the reduced motility and decreased intracellular asparagine (Table 1) in *atg5*-KO tumor cells, we then postulated that defective autophagy suppresses tumor cell motility, at least in part, by reducing the availability of asparagine generated through autophagic recycling. To test this hypothesis, we systematically compared the response of *Atg5*-WT and *atg5*-KO tumor cells to supplementation of asparagine/aspartate or NAC using the in vitro wound scratch assay (Figure 6A), cell migration assay (Figure 6B), and cell invasion assay (Figure 6C). The results confirmed that depletion of ATG5 suppresses cell motility, migration, and invasion, respectively, independent of the effect on cell proliferation. Furthermore, we ruled out the involvement of ROS in promoting SDC cell motility, as supplementation with the ROS scavenger NAC (10 mM) did not affect the motility of tumor cells from either genotype (Figure 6A, top panel). Instead, supplementation with asparagine, but not aspartate, reverted the migration of *atg5*-KO cells in an in vitro wound scratch assay to a level similar to *Atg5*-WT cells (Figure 6A, bottom panel). Lastly, we extended our observation to MDA-MB-231 breast cancer cells, which carry KRAS mutation as well. Similar to our results with SDC tumor cells, knockdown of ATG5 in KRAS-mutated MDA-MB-231 cells compromised motility in the in vitro wound closure assay (Figure S7B). Likewise, knockdown of ASNS reduced cell motility, which was salvaged by supplementation with exogenous asparagine, but not aspartate, in both autophagy-competent MDA-MB-231 (Figure 6D) and *Atg5*-WT SDC cells (Figure S7C). However, no difference in wound closure was detected comparing control and *Asns*-silenced *atg5*-KO SDC cells (Figure S7C). The lack of effect by aspartate might reflect the poor cellular uptake (Figure 6A–D). These results suggest that the higher autophagy-competent tumor cell motility rate, compared to corresponding autophagy-compromised cells, is likely due to greater asparagine availability. Furthermore, impaired mitochondrial dynamics and the reduced cell motility were correlated in KRAS^{G12V};*atg5*^{Δ/Δ} cells, since silencing *Mff* reverted the in vitro scratch wound assay (Figure S7A).

ASNS overexpression is associated with poor prognosis

In order to further extend our understanding of asparagine or ASNS in stress response and homeostasis control in human cancers, we determined ASNS representations and clinical implications. First, we cross-referenced the ASNS expression pattern in multiple human cancers using a collection of publicly available datasets. Elevated ASNS expression in primary tumors, relative to normal tissues, was consistently detected across human cancer types, including breast cancer, in The Cancer Genome Atlas (TCGA) Pan-Cancer RNA-seq dataset [22] (Figure 7A). We next compared the ASNS expression levels across various breast cancer subtypes (triple negative [TNBC], ERBB2/HER2⁺ [erb-b2 receptor tyrosine kinase 2] and others), with that of normal breast tissues in the TCGA breast cancer (BRCA) cohort, based on samples' IHC information. Notably, the TNBC samples showed the highest ASNS

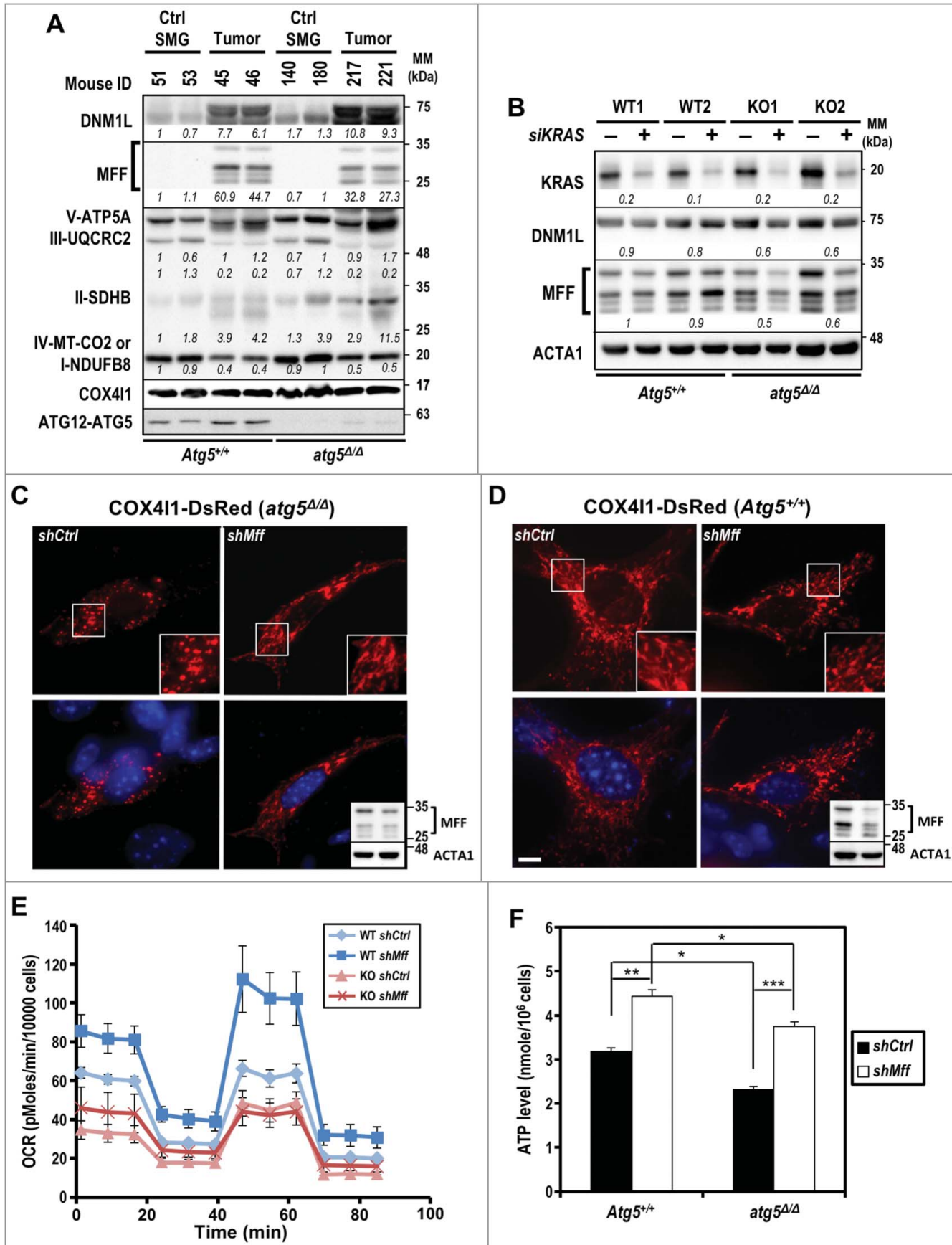


Figure 4. Impaired mitochondrial dynamics in autophagy-compromised tumor cells. (A) Increased abundance of mitochondrial fission-related proteins, DNM1L and MFF, in KRAS-transformed tumors. Equal amounts of total tissue lysates prepared from control and tumor-induced mice (d 24) of both genotypes were subjected to western blot analyses as indicated. Levels of 5 oxidative phosphorylation enzyme complexes subunits including NDUFB8 (complex I), SDHB (complex II), UQCRC2 (complex III), MT-CO2 (complex IV) and ATP5A (complex V) were detected with total OXPOHS rodent WB antibody cocktail. Mitochondrial complex IV is shown as a loading control. A

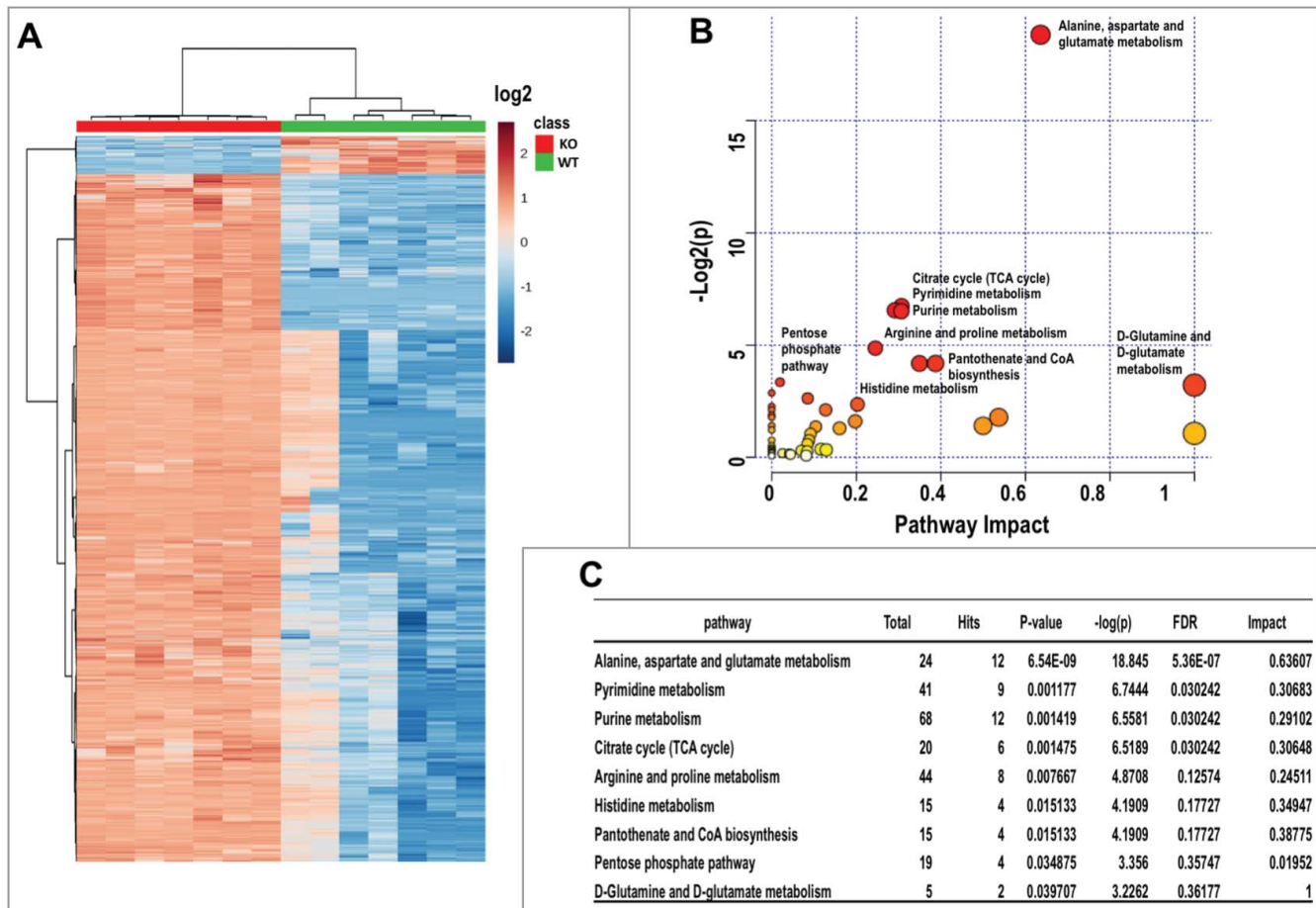


Figure 5. Metabolomics analysis of $KRAS^{G12V};Atg5^{+/+}$ and $KRAS^{G12V};atg5^{\Delta/\Delta}$ SDC cells. (A) Clustering analysis and Heatmap of metabolites from both $KRAS^{G12V};Atg5^{+/+}$ and $KRAS^{G12V};atg5^{\Delta/\Delta}$ SDC cells. Seven replicates were included in each group. Data is shown in log₂ scale. (B) Overview of pathway analysis. Scatter plot represents *p*-value and pathway impact from pathway topology analysis of the differentially expressed metabolites from $KRAS^{G12V};Atg5^{+/+}$ and $KRAS^{G12V};atg5^{\Delta/\Delta}$ SDC cells. The color and size of each node is based on its *p*-value and pathway impact value, respectively. Pathways with statistical significance ($p < 0.05$) are shown in red. (C) The numerical details of results from the pathway analysis shown in (B). The cut-off *p*-value is set at $p < 0.05$. FDR; false discovery rate.

expression level (3.3-fold increase over normal) compared with the 1.67- and 1.47-fold increase observed in the ERBB2⁺ subtype and others, respectively (Figure 7B). We then validated the observation, using another breast cancer meta-analysis dataset from The Netherlands Cancer Institute (NKI [23]). The ASNS expression levels of 4 Pam50 subtypes (determined by Affymetrix expression arrays, including basal, HER2-like, luminal A, and luminal B) were compared to the expression levels in the normal-like subtype. Again, the basal type, which largely overlaps with TNBC, displayed the highest ASNS expression (1.61-fold increase compared with the 1.29-, 0.97-, and 1.27-fold increase over normal observed for HER2-like, luminal A, and luminal B, respectively) (Figure 7C).

Active tumor cell migration is a prerequisite for invasion and metastasis. Because our observation suggested that extracellular asparagine supplementation rescues motility in autophagy-compromised and/or ASNS-KD SDC tumor cells (Figure 6A-C and S7C), as well as in ASNS-KD MDA-MB-231 cells (Figure 6D), we probed the correlation of ASNS expression with breast cancer brain metastasis. As expected, ASNS expression levels in breast-to-brain metastatic samples showed an average of 2.24-fold increase compared with normal breast tissues, using a National Center for Biotechnology Information-Gene Expression Omnibus (NCBI-GEO) dataset (GSE52604 [24]) (Figure 7D). Finally, we evaluated the correlation between ASNS expression levels and the breast cancer metastasis

representative western blot of 2 mice per group is shown. Relative abundance of each protein is calculated by designating the level in control mouse (ID 51) as 1 after normalization with COX41 and shown in italics. Multiple bands in MFF western blot represent splice variants of MFF [58]. (B) Knockdown of *KRAS* decreases MFF and DNM1L levels in $KRAS^{G12V};atg5^{\Delta/\Delta}$ cells. Primary tumor cells were transfected with siRNA against human *KRAS* at 48 h prior to analyses. Relative fold change (*siKRAS* over Control) of each sample is calculated by designating the densitometry tracing value in the control as 1 after normalization with ACTA1, as shown in italics. (C and D) Knockdown of MFF reverts the fragmented mitochondrial phenotype notably in $KRAS^{G12V};atg5^{\Delta/\Delta}$ (C) compared to $KRAS^{G12V};Atg5^{+/+}$ (D) cells. Knockdown of MFF is shown by western blot analysis (upper panel, lower-right inset) with ACTA1 serving as a loading control (lower panel, lower-right inset). Multiple bands of MFF are likely due to alternative splicing. Scale bar: 10 μ m. (E) Oxygen consumption rate (OCR) was measured in control (*shCtrl*) and *Mff*-KD (*shMff*) $KRAS^{G12V};Atg5^{+/+}$ (WT) and $KRAS^{G12V};atg5^{\Delta/\Delta}$ (KO) cells. Data are shown as the mean \pm S.D.; $n = 3$. (F) Levels of ATP were measured in control and *Mff*-KD $KRAS^{G12V};Atg5^{+/+}$ and $KRAS^{G12V};atg5^{\Delta/\Delta}$ cells. The ATP levels were normalized to cell number. Data are shown as mean \pm S.D.; $n = 3$. *: $p < 0.05$; **: $p < 0.01$; ***: $p < 0.001$ (Student *t* test, 2-tailed, unpaired).

Table 1. Relative intracellular concentration of amino acids from KRAS^{G12V};Atg5^{+/+} and KRAS^{G12V};atg5^{Δ/Δ} SDC tumor cells.

| Amino acid | Ratio (Atg5 ^{Δ/Δ} :Atg5 ^{+/+}) | p-value |
|------------|---|---------|
| Ala | 0.73 | 0.031 |
| Arg | 0.55 | <0.001 |
| Asn | 0.70 | 0.012 |
| Asp | 0.70 | 0.039 |
| Cys-Cys | 1.02 | 0.949 |
| Gln | 1.69 | 0.035 |
| Glu | 0.96 | 0.887 |
| Gly | 0.80 | 0.314 |
| His | 0.68 | 0.047 |
| Ile | 0.71 | 0.019 |
| Leu | 0.74 | 0.040 |
| Lys | 0.55 | <0.001 |
| Met | 0.67 | 0.025 |
| Phe | 0.70 | 0.052 |
| Pro | 0.63 | 0.007 |
| Ser | 0.66 | 0.019 |
| Thr | 0.76 | 0.120 |
| Trp | 0.95 | 0.700 |
| Tyr | 0.79 | 0.150 |
| Val | 0.71 | 0.010 |

Essential amino acids: histidine, isoleucine, leucine, lysine, methionine, phenylalanine, threonine, tryptophan and valine.

Nonessential amino acids: alanine, arginine, asparagine, aspartic acid, cysteine, glutamic acid, glutamine, glycine, proline, serine, and tyrosine.

outcomes using 3 different NCBI-GEO datasets (GSE25066 [25], GSE17705 [26], and GSE12276 [27]). Kaplan-Meier analyses revealed that the high ASNS expression was significantly associated with worse distal metastasis-free survival outcome compared with the low expression group (Log-rank *p*-value <0.01 for all 3 datasets; Figure 7E-G). In addition to breast cancer, elevated expression of ASNS was significantly associated with poor overall survival in multiple human cancers (Figure S8). To link expression level between *ATG5* and *ASNS*, TCGA datasets were analyzed and there is a positive correlation between the expression of these 2 genes in both breast cancer and head and neck cancer datasets (Figure S9A and S9B). Further, we examined the same sets of distal metastasis-free survival of breast cancer cohorts (Figure 7E-G) and likewise found positive correlation between *ATG5* and *ASNS* expression (Figure S9C). Altogether, our data support a model wherein compromised autophagy leads to compensatory increase in *Asns* expression, which produces some asparagine, however, insufficient to offset the loss in asparagine output from autophagic recycling, in order to meet the metabolic demands of tumor growth. Together, we conclude that the combined asparagine deficiency and excessive mitochondrial fragmentation reduce proliferation, migration and invasion of autophagy-impaired tumor cells, conferring a survival advantage on tumor-bearing KRAS^{G12V};atg5^{Δ/Δ} mice (Figure 1F).

Discussion

Our study revealed a widespread yet specific homeostatic control of asparagine availability to promote tumor cell motility and the ability of activated autophagy to shift mitochondrial constraints, suggesting that autophagy may have a direct relevance to the oncogenic KRAS-mediated metabolic reprogramming. The importance of autophagy in cancer, whether autophagy promotes or inhibits cancer, depends on the timing and context [28,29]. Insight into the mechanisms linking

autophagy to tumor progression is needed to resolve such a complex role of autophagy in cancer. We investigated the biological outcome and key metabolic events that autophagy regulates in transgenic mice expressing conditionally-activated oncogenic KRAS with concomitant ablation of *Atg5*. These autophagy-deficient mice undergo rapid onset of ductal hyperplasia and dysplasia; however, which persists and progresses into invasive SDC at a reduced rate. An overall extended survival of KRAS^{G12V};atg5^{Δ/Δ} tumor-bearing transgenic mice, compared to KRAS^{G12V};Atg5^{+/+} mice, was demonstrated. Our study further identified impaired asparagine availability and mitochondrial integrity as important metabolic barriers to autophagy-compromised, KRAS-transformed tumor cell migration and invasion. These results support a model wherein autophagy fuels cellular metabolism by maintaining mitochondrial dynamics and providing asparagine to reinforce tumor cell migration and promote invasion, thereby accelerating the progression of KRAS^{G12V}-transformed tumors (Figure S10).

We found that disruption of autophagy promotes excessive mitochondrial fission phenotype and slows tumor cell migration in SDC. Mitochondrial fission proteins play essential roles in mitochondrial function [30] and KRAS-driven tumorigenesis [31-33]. It is possible that the excessive mitochondrial fragmentation in the *atg5*-KO tumors causes the observed decrease in oxidative phosphorylation and ATP production, thereby impairing ATP-dependent tumor cell migration. Conceivably, the compromised autophagy failed to remove fissioned mitochondria, exacerbating mitochondrial over-fission phenotype. Furthermore, this phenotype may result from nutrient depletion-associated kinase activation. AMPK (AMP-activated protein kinase) [34,35] and MAPK [31,32] phosphorylate the mitochondrial fission proteins MFF and DNMI1L, respectively, to regulate mitochondrial dynamics and, in the case of DNMI1L, promote RAS-induced tumor growth and/or tumorigenesis [31-33]. Our report on the partial alleviation of excessive mitochondrial fragmentations and increased ATP production by *shMff* in *atg5*-KO tumor cells supports a multifactorial nature of autophagy and mitochondrial dynamics. Perhaps most importantly, the observation that excessive mitochondrial fission interfered with *atg5*-KO, but not *Atg5*-WT, tumor cell migration assigns a key role of mitochondrial equilibrium in the regulation of cell metabolism and migration in the context of stress from the absence of autophagy.

In our oncogenic KRAS model, tumor cells' demand for asparagine for both anabolic process and tumor cell migration, together with our systematic analyses on the overexpression of *ASNS* across multiple different cancer types and impact on clinical outcome, argue that increased asparagine availability by autophagy or *ASNS* overexpression escalates tumor progression. Autophagy-mediated degradation of intracellular components provides tumor cells with recycled nutrients, including amino acids [36,37], and rapidly dividing tumor cells are thought to be "addicted" to autophagy to meet their anabolic needs [38,39]. Moreover, activated KRAS increases protein scavenging via macropinocytosis [40,41] or macropinocytosis-associated autophagy [42] to supply nutrients. We have previously shown that, compared to *Atg5*-WT mouse embryonic fibroblasts (MEFs), *atg5*-KO MEFs have lower levels of intracellular nonessential amino acids, including asparagine [43]. In

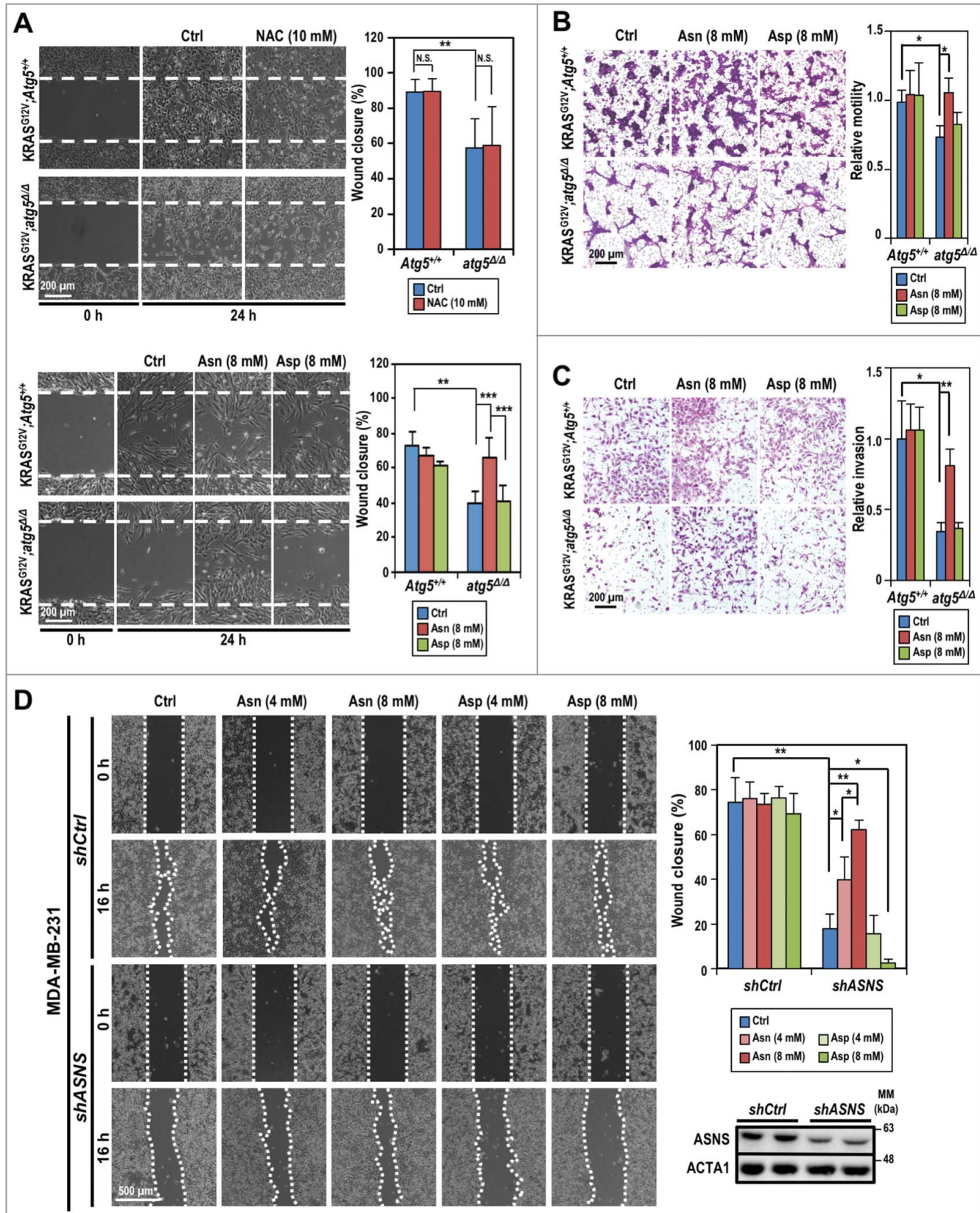


Figure 6. Compromised autophagy decreases tumor cell invasion. (A) Asparagine promotes $KRAS^{G12V};atg5^{\Delta/\Delta}$ cell motility as shown by in vitro scratch assays. Live cell images were taken right after the “scratches” were created (0 h) and at 24 h post-treatment (or not) of NAC (10 mM, upper left panels), and asparagine/aspartate (8 mM, lower left panels). Quantification of percent wound closure (right panels) was conducted by measuring the decrease in the denuded area at 24 h ($n = 3$). (B) Asparagine promotes $KRAS^{G12V};atg5^{\Delta/\Delta}$ cell migration as shown by transwell migration assays. Standard transwell migration assays with a full media supplemented with Asn (8 mM), Asp (8 mM) or without (Ctrl) were performed. Following 24 h incubation, the cells on the other side of the membrane were fixed with ice cold methanol and stained with crystal violet. Representative images (left panel) and quantification (right panel) are shown ($n = 3$). (C) Autophagy is required for SDC cell invasion. In the invasion assay, $KRAS^{G12V};Atg5^{+/+}$ and $KRAS^{G12V};atg5^{\Delta/\Delta}$ tumor cells were grown as in (B) and quantified for Matrigel invasion using collagen I as a chemoattractant. Representative images (left panel) and quantification (right panel) are shown ($n = 3$). (D) Knockdown of *ASNS* reduces MDA-MB-231 cell motility while supplementation of asparagine reverses the

this study, we found that autophagy disruption slowed KRAS-driven tumor cell migration, at least in part, by limiting asparagine availability despite a compensatory increased *Asns* expression (Figure S6D). In contrast, the glutamine level increased in these tumor cells with compromised autophagy (Table 1; Figure S6A), further attesting the critical role for asparagine in supporting tumor progression [44,45]. Consistent with our findings, asparagine is one of 4 amino acids significantly decreased in the tumor core regions of xenografted human melanoma [46] and among the most strongly depleted metabolites in human pancreatic tumors [41]. In line with our data, other studies have shown that asparagine levels regulate other amino acids homeostasis [47,48], a mechanism that likely helps tumor cells in meeting the anabolic demand. The requirement of millimolar range of asparagine to rescue the phenotype of compromised autophagy or ASNS-knockdown suggests the inefficiency of asparagine transport across cell membrane and/or the importance of asparagine compartmentalization. The latter possibility is supported by the lack of clinical efficacy of asparagine-depleting asparaginase therapy in treatment of cancers expressing high levels of ASNS [49].

Conceptually, our results are consistent with the observations that asparagine serves as a cellular sensor of reduced TCA cycle intermediates or nitrogen availability [45,50] to coordinate protein and nucleotide synthesis [47]. Although whether there is a direct functional dependence between endogenous asparagine level and mitochondria dynamics remains unclear and warrants further studies, our findings provide a mechanistic explanation for the broader notion that autophagy promotes oncogenic RAS-driven invasion and complement other alternatives that autophagy enables focal adhesion disassembly in motile cells or provides secreted factors, such as IL6 in a context-dependent manner [51]. Finally, the availability of asparagine in tumor cells is tightly co-regulated by the combined actions of degradative and recycling functions of autophagy and elevated ASNS expression; whether these 2 biological processes are co-regulated is yet to be determined. However, positive correlation between expression of *ATG5* and ASNS were found in selected cancers (Figure S9). Interestingly, The Human Protein Atlas (v18; www.proteinatlas.org) analyzed the proteome of 17 major cancer types and high expressions of *ATG5* and ASNS, respectively, were both unfavorably associated with survival rate of patients with renal and liver cancer, as demonstrated by Kaplan-Meier plots. Amino acid starvation is known to induce autophagy while ASNS is activated by ATF4 (activating transcription factor 4) following amino acid deprivation [48]. To meet the demand from the highly proliferative cancer cells, it is perhaps not surprising to find upregulations and unfavorable associations with certain types of human cancer for both. ASNS was likely compensatorily elevated due to amino acid depletion in our autophagy-compromised SDC tumor cells, however, its increased expression might not have been sufficient to offset declined intracellular asparagine as a

result of autophagy deficiency. Consequently, the overall survival was lower in mice bearing autophagy compromised SDC tumor even when ASNS was upregulated in tumors. These results implicate asparagine availability as a common metabolic vulnerability in multiple cancers and propose that ASNS inhibition, combined with autophagy suppression, such as by chloroquine [52], and/or other therapies, may represent a personalized strategy for managing ASNS-overexpressing tumors. In summary, our findings reveal that low asparagine and excessive mitochondrial fragmentation represent previously unrecognized metabolic barriers against malignant KRAS-driven tumor invasion potential in the context of compromised autophagy. The association between the ASNS overexpression and the poor clinical outcomes of multiple cancers suggests that the potential of limiting asparagine availability, including by autophagy inhibitors, should be further tested for impeding tumor cell migration and progression.

Materials and Methods

Mouse breeding

Animal care and experimental procedures were conducted in accordance with the guidelines and regulations of the Institutional Animal Care and Use Committee at City of Hope. The Institutional Animal Care and Use Committee at City of Hope approved all animal experiments. All mouse colonies were maintained in pathogen-free barrier facilities. *LGL-KRAS^{G12V}* and *Ela-CreERT* transgenic mice were described previously [11]. *LGL-KRAS^{G12V}* mice, *Ela-CreERT* mice, and *Atg5^{lox/lox}* mice [13] were crossed to derive *Ela-CreERT;LGL-KRAS^{G12V};Atg5^{lox/lox}* (*KRAS^{G12V};Atg5^{lox/lox}*), *Ela-CreERT;LGL-KRAS^{G12V};Atg5^{lox/+}* (*KRAS^{G12V};Atg5^{lox/+}*), and *Ela-CreERT;LGL-KRAS^{G12V};Atg5^{+/+}* (*KRAS^{G12V};Atg5^{+/+}*) mice. Mice at 8- to 10-wk of age were gavaged with tamoxifen (3 mg/40 g body weight) (MilliporeSigma, T5648) or vehicle daily for 5 consecutive d. Genotyping was conducted as we described previously [11,13].

Tissue preparation and characterization

Salivary glands were harvested at the indicated time after the first day of tamoxifen feeding. Tumor masses were excised *en bloc* with adjacent tissues. Tissue samples were fixed in 10% neutral-buffered formalin (MilliporeSigma, HT501128) for 48 h. Tissue embedding, sectioning, and staining with modified Mayer's hematoxylin (American MasterTech, HXMMHGAL) and eosin Y stain (American MasterTech, STE0157) were performed in the City of Hope Pathology Core. Briefly, after deparaffinization and rehydration, the sections were stained with modified Mayer's hematoxylin for 4 min, rinsed in tap water; and destained with 0.3% acid alcohol. After rinsing in tap water, sections were stained with eosin Y for 2 min, followed by dehydration, clearing, and mounting.

ASNS-KD effect. MDA-MB-231 cells (*shCtrl* or *shASNS*) were incubated in full media or full media supplemented with the indicated concentrations of asparagine or aspartate after the wounds were created. Representative images taken at 0 and 16 h post-wounding are shown (left panel). Quantification of wound closure (%) is shown (upper right panel). Western analysis confirmed knockdown of ASNS by *shASNS* (lower right panel). ACTA1 serves as a loading control. *: $p < 0.05$; **: $p < 0.01$; ***: $p < 0.001$, N.S.: not significant (Student *t* test, 2-tailed, unpaired).

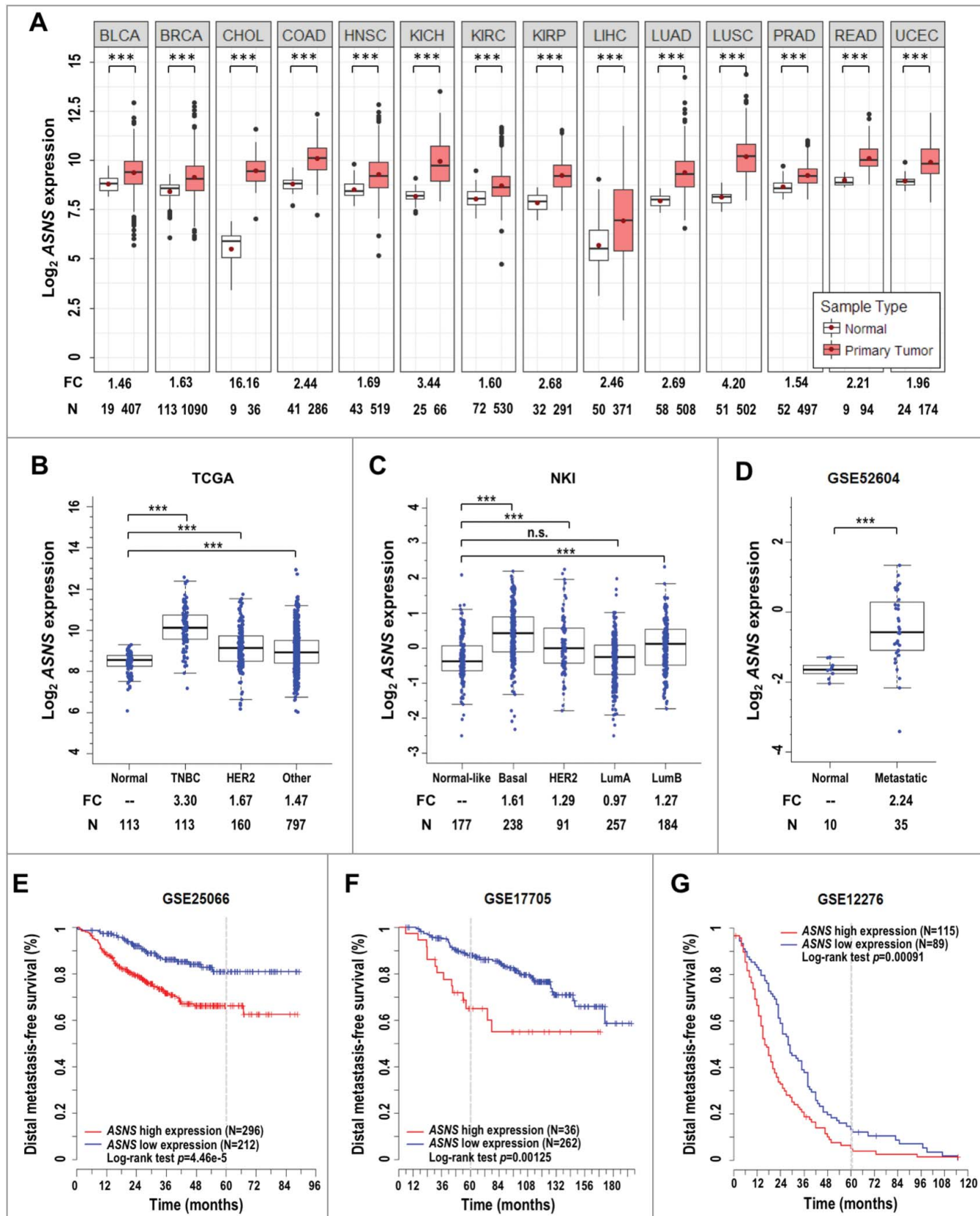


Figure 7. Association of *ASNS* expression with clinical prognosis. (A) *ASNS* is overexpressed in human cancers. Red dots in standard boxplots indicate the average expression values. Fold change (FC) of normalized expression values and the number (N) of samples are labeled at the bottom. *P*-values between groups were determined using Welch's *t* test. ***: $p < 0.001$; BLCA, bladder urothelial carcinoma; BRCA, breast invasive carcinoma; CHOL, cholangiocarcinoma; COAD, colon adenocarcinoma; HNSC, head and neck squamous cell carcinoma; KICH, kidney chromophobe; KIRC, kidney renal clear cell carcinoma; KIRP, kidney renal papillary cell carcinoma; LIHC, liver hepatocellular carcinoma; LUAD, lung adenocarcinoma; LUSC, lung squamous cell carcinoma; PRAD, prostate adenocarcinoma; READ, rectal adenocarcinoma; UCEC, uterine corpus endometrial carcinoma. (B) *ASNS* is overexpressed in tumor samples of all breast cancer subtypes, compared to normal breast tissues, in the TCGA dataset. Triple-negative breast cancer (TNBC), HER2⁺ and other subtypes were determined by immunohistochemistry. (C) *ASNS* expression levels across Pam50 breast cancer subtypes (basal,

Immunohistochemistry and quantification

Immunohistochemistry (IHC) was performed using Citrate-based Antigen Unmasking Solution (Vector Laboratories, H-3300), Vectastain Elite ABC-HRP Kit (Vector Laboratories, PK-6100), Avidin/Biotin Blocking Kit (Vector Laboratories, SP-2001), and ImmPACT DAB Peroxidase (HRP) Substrate Kit (Vector Laboratories, SK-4105) according to the manufacturer's protocols. Briefly, the paraffin sections were deparaffinized and hydrated through xylenes and graded alcohol solutions. The tissue slides were pressure-cooked in citrate-based unmasking solution for 30 min and washed in phosphate-buffered saline (PBS; 137 mM NaCl, 2.7 mM KCl, 10 mM Na₂HPO₄, 1.8 mM KH₂PO₄, pH 7.4) for 5 min, followed by quenching of endogenous peroxidase activity in H₂O₂ (0.3%; MilliporeSigma, H1009) for 30 min. The slides were then blocked for 20 min with a mixture of Avidin D solution and diluted normal blocking serum, which was prepared from the species in which the secondary antibody is made. The slides were then incubated with a mixture of primary antibody and biotin solution for 30 min and washed in buffer 3 times. The slides were incubated in the Vector biotinylated secondary antibody for 30 min, washed for 5 min, and then incubated in Vectastain Elite ABC Reagent for 30 min. After being washed for 5 min, the slides were processed with the DAB Substrate Kit. The slides were counter-stained with hematoxylin, dehydrated, and mounted. The cells that stained positive by IHC in 3 non-overlapping 5 X or 10 X fields were counted with Image-Pro Premier 9.0 (Media Cybernetics) and slides from at least 4 mice were included in each group.

Primary tumor cell isolation

Isolation and culture of primary tumor cells was conducted as previously described [53]. In brief, d 23 and d 24 tumors were minced into small pieces and digested for up to 60 min at 37°C in digestion medium containing collagenase (1 mg/ml; MilliporeSigma, C6885), hyaluronidase (100 units/ml; MilliporeSigma, H3506), DNase I (50 µg/ml; MilliporeSigma, D4527), bovine serum albumin (1 mg/ml; MilliporeSigma, A2153), HEPES (pH 7.3, 20 mM; Corning, 25-060-CI) in Dulbecco's Modified Eagle's Medium/Ham's F-12 50/50 Mix (Corning, 16-405-CV). The suspension of digested tumor cells was passed through a 100 µm sieve to remove the remaining tissue chunks. The red blood cells were lysed by incubating cell suspensions in 1X red blood cell lysis buffer (155 mM NH₄Cl, 12 mM NaHCO₃, 0.1 mM EDTA, pH 7.3) for 3 min on ice. The resulting cells were plated on collagen I-coated dishes (Corning, 354450), and maintained in a medium consisting of Dulbecco's Modified Eagle's Medium (Corning, 10-013-CV) with fetal bovine serum (10%; Thermo Fisher Scientific, 10437028), L-glutamine (5 mM; Thermo Fisher Scientific, A2916801), hydrocortisone (400 ng/ml; MilliporeSigma, H0888), insulin (5 µg/

ml; Thermo Fisher Scientific, 12585014), EGF (20 ng/ml; Thermo Fisher Scientific, PHG0311), HEPES (15 mM; Thermo Fisher Scientific, 15630080) and antibiotic-antimycotic (1X; Thermo Fisher Scientific, 15240112). After 1 to 2 wk of incubation, colonies of the GFP-negative tumor cells were manually picked and transfer to new cell culture dishes.

Antibodies and reagents

The primary antibodies used were: rabbit polyclonal anti-MKI67/Ki67 antibody (abcam, ab15580), rabbit polyclonal anti-pan-KRT/cytokeratin antibody (abcam, ab9377), mouse monoclonal anti-COX4I1/COX IV antibody (abcam, ab14744), rabbit polyclonal anti-SNAI1/SNAIL + SNAI2/SLUG antibody (abcam, ab180714), rabbit polyclonal anti-phospho-H3F3/histone H3 (Ser10) antibody (MilliporeSigma, 06-570), mouse monoclonal anti-actin antibody (MilliporeSigma, MAB1501R), rabbit anti-CDKN2A/p16 antibody (Santa Cruz Biotechnology, sc-1207) and anti-CDKN1A/p21 antibody (Santa Cruz Biotechnology, sc-6246), rabbit anti-SQSTM1/p62 antibody (Proteintech Group, 18420-1-AP), rabbit anti-ASNS antibody (Proteintech Group, 14681-1-AP), rabbit anti-MFF antibody (Proteintech Group, 17090-1-AP), mitoprofile total OXPOHS rodent WB antibody cocktail (abcam, ab110413), rabbit anti-DLP1 antibody (BD Biosciences, BD 611112), mouse anti-human KRAS antibody (Bio-Rad, MCA3223Z), rabbit anti-ATG5 antibody (Novus Biologicals, NB110-53818), and rabbit anti-LC3B antibody (Novus Biologicals, NB100-2220).

N-acetyl-L-cysteine (A7250), L-asparagine (A4159), and aspartic acid (A8959) were from MilliporeSigma. siRNA against human *KRAS* was obtained from MilliporeSigma (SASI_Hs02_00361210) and siRNA against mouse *Asns* was from Santa Cruz Biotechnology (Santa Cruz Biotechnology, sc-60213). Transfections of siRNA were performed with Lipofectamine RNAiMAX transfection reagent (ThermoFisher Scientific, 13778150), according to the manufacturer's instructions.

RNA extraction and qRT-PCR

Total RNA was prepared from primary tumor cells with RNeasy Mini Kit (Qiagen, 74104), following the manufacturer's instructions. The concentration and purity of RNA were measured by NanoDrop spectrophotometry (NanoDrop Technologies). Real-time reverse-transcription PCR (qRT-PCR) was conducted as we described previously [13]. The sequence of the primers used for qPCR: *Atg5* forward primer 5'-CAGAAGGT-TATGAGACAAGAAGATG-3', reverse primer 5'-TGGATG-GACAGTGTAGAAGGTC-3'; *Asns* forward primer 5'-GCAG TGTCTGAGTGCCATGAA-3', reverse primer 5'-TCTTATCG GCTGCATTCCAAAC-3'; *Rn18s rRNA* forward primer 5'-CG GCGACGACCCATTCGAAC-3', reverse primer 5'-GAATC-GAACCTGATTCCTCCGTC-3'.

HER2-like [HER2], luminal A [LumA], and luminal B [LumB]) compared with normal-like subtype using the Netherlands Cancer Institute (NKI) breast cancer dataset, n.s., not significant. (D) Elevated *ASNS* expression in breast-to-brain metastatic samples, compared with normal breast tissues, in an NCBI-GEO dataset (GSE52604). (E, F and G) Kaplan-Meier analyses of the distal metastasis-free survival of 3 breast cancer cohorts, based on *ASNS* expression (GSE25066, GSE17705, and GSE12276). The analyses employ log-rank score tests to identify the optimal cut-point for grouping patients. A gray dotted line shows the 5-y mark. The *p*-value for log-rank test is shown.

Western blot analyses

Whole tissue lysates were prepared using cOmplete Protease Inhibitor Cocktail (MilliporeSigma, 4693116001) supplemented lysis buffer from Qproteome Mammalian Protein Prep Kit (Qiagen, 37901), according to the protocol from the manufacturer. Whole cell lysates were prepared by directly lysing cells in 1x Laemmli buffer (45 mM Tris-HCl, pH 6.8, 10% glycerol, 1% SDS, 50 mM DTT, 0.01% bromophenol blue) with protease inhibitor. Equal amounts of total protein were subjected to SDS-PAGE and immunoblotted with primary antibodies of interest followed by horseradish peroxidase conjugated secondary antibody following manufacturer's instruction. After chemiluminescent reaction, blots were visualized with a Chemi-Doc Touch Imaging System (Bio-Rad). The signal intensities of the captured images were analyzed with Image Lab Software (Bio-Rad, version 5.2.1). Results of western analyses shown are representatives of at least 3 independent experiments.

Measurement of intact cellular respiration and glycolytic function

Mitochondrial OCR and ECAR were measured by the Agilent Seahorse XF24 Extracellular Flux Analyzer using Seahorse XF24 FluxPaks (Agilent, 100850-001) according to the manufacturer's instructions. Briefly, 1×10^5 cells were seeded in collagen I-coated XF24 cell culture microplates overnight. On the next day, the cells were washed and incubated with Seahorse XF base medium (Agilent, 102353-100) supplemented with glucose (25 mM; MilliporeSigma, G7021) and sodium pyruvate (1 mM; Thermo Fisher Scientific, 11360070), pH 7.4. OCR was assayed by sequential injections of oligomycin A (1 μ M; MilliporeSigma, 75351), FCCP (0.5 μ M; MilliporeSigma, C2920) and rotenone (2.5 μ M; MilliporeSigma, R8875). ECAR was assayed by sequential addition of glucose (10 mM), oligomycin (1 μ M), and 2-deoxyglucose (2-DG, 100 mM; MilliporeSigma, D6134). After the measurements, the cells were trypsinized, and the cell numbers were counted for normalization. The data are presented as mean \pm S.D..

NAC treatment and intracellular ROS measurement

ROS measurement was performed using the cell-permeant reagent 2',7'-dichlorofluorescein diacetate (DCFDA; MilliporeSigma, D6883), as described previously [54]. Briefly, the cells were stained with DCFDA (1 μ M) for 30 min and the resulting DCF was analyzed by flow cytometry with a maximum emission \sim 530 nm (Beckman Coulter Gallios or Accuri C6 flow cytometer). For NAC treatment, the cells were seeded at 50% confluence in 12-well plates and incubated with full media supplemented with NAC (5 mM or 10 mM) for 24 h before DCFDA staining.

ATP assay

The cellular ATP level was measured using the ENLITEN ATP Assay System (Promega, FF2000) following the manufacturer's manual. In brief, the cells were grown to sub-confluence and harvested in ice-cold PBS by scraping. ATP was extracted by

adding 5% trichloroacetic acid (TCA; J.T. Baker, 0414-04) and then the reaction was neutralized with Tris-acetate-EDTA buffer (100 mM Tris, 2mM EDTA, pH 7.75). The extracts were further diluted 1:100, and an equal volume of rL/L reagent was added to measure the luminescence using a TD-20e luminometer (Turner Biosystem). An ATP standard curve was generated according to the manufacturer's instructions. The ATP levels were normalized to the cell number.

Mitochondrial membrane potential

The cells were stained with 3,3'-dihexyloxycarbocyanine iodide (DiOC6, 10 nM; MilliporeSigma, 318426) for 30 min at room temperature and the fluorescence intensity was analyzed by flow cytometry using an Accuri C6 flow cytometer (BD Biosciences).

Cell migration assay

The in vitro wound healing assay was performed as described [55]. Briefly, the cells were grown to confluence in 35 mm dishes and the cell monolayer was scratched in a straight line with a p200 pipet tip. The images were acquired with a phase-contrast microscope at the time of scraping (0 h) and again after 24 h of incubation. The rate of cell migration was calculated as a percentage of wound closure using Image-Pro Premier software. All experiments were repeated 3 times.

Transwell migration assay

The Transwell migration assay was performed in triplicate using Transwell-permeable support inserts with 8 μ m pores (Corning, 3464). Both sides of the insert membrane were pre-coated with collagen I (ThermoFisher, A1048301) before cell seeding. The cells (1×10^5) were seeded in the upper chamber in full media. Full media, supplemented with collagen I (40 μ g/ml) as a chemoattractant, was placed in the lower well. After 24 h of incubation, the cells in the upper chamber were removed using a cotton swab, and the migrated cells from the underside of the membrane were fixed with ice-cold methanol and stained with crystal violet (Aqua Solutions, C8126). The cell numbers from 5 random fields from each experimental group were counted.

Invasion assay

Cell invasion was determined using BioCoat Matrigel invasion chambers (Corning, 354480). Briefly, the cells (1×10^5) were seeded in the upper chamber in full media after the chambers were rehydrated. The lower chamber was filled with full media supplemented with collagen I (40 μ g/ml). After 24 h of incubation, the cells that invaded through the Matrigel-coated membrane were stained with crystal violet and counted.

Nutrient depletion and cell viability

The acid phosphatase (ACP) assay was used to measure cell viability, as described previously [13]. Briefly, 5×10^3 cells/well were seeded into 96-well plates and incubated in the presence

of different concentrations of glucose or glutamine for 48 h. The cells were then washed with PBS and incubated with *p*-nitrophenyl phosphate disodium hexahydrate (5 mM; MilliporeSigma, N4645) in 100 μ l of sodium acetate (0.1 M; Fisher Chemical, S210-500) and Triton X-100 (0.1%; Fisher Bioreagents, BP151-100), pH 5.0, for 30 min at 37°C. The reaction was stopped with the addition of NaOH (10 μ l, 1 N; Fisher Chemical, S318-500) and absorbance was measured at 405 nm using a microplate reader.

Cell proliferation assay

Cells were seeded into 24-well plates at 2×10^4 cells per well. Asparagine was added during cell seeding if required. Cell viability was measured every 24 h to monitor cell growth by using the ACP assay. Experiments were repeated 3 times.

Apoptosis assay

Apoptosis was analyzed by ANXA5/annexin V-propidium iodide (PI) staining (BD Pharmingen, 556547) following the manufacturer's instructions. In brief, *Atg5*-WT and *atg5*-KO cells were trypsinized and diluted to 1×10^6 cells/ml. The cells (100 μ l) were incubated with ANXA5 and PI at room temperature in the dark for 15 min and analyzed with an Accuri C6 flow cytometer.

Metabolite extraction and mass spectrometry

Atg5-WT and *atg5*-KO cells were allowed to grow to 70% confluence and harvested in ice-cold PBS by scraping. The cell pellets were then snap frozen in liquid nitrogen and stored at -80°C. Seven biological replicates, consisting of 1×10^7 cells, were included in each group. The metabolite extraction, mass spectrometry analysis, and data analysis were carried out at the Center for Metabolomics and Mass Spectrometry at The Scripps Research Institute. In brief, metabolite extraction was done by adding 80% methanol (400 μ l) to each cell pellet, vortexed, and placed in liquid nitrogen for 10 min. The samples were then allowed to thaw and sonicated for 10 min. The freeze/thaw cycle was repeated 3 times before centrifuging the samples at 16,000 \times g for 10 min. The supernatant was harvested and evaporated to dryness in a SpeedVac at room temperature. The samples were reconstituted in 50% methanol (100 μ l), sonicated for 15 min, and then transferred to autosampler vials with inert inserts.

The negative mode analysis was performed on a 6538 Q-TOF mass spectrometer (Agilent) coupled with an 1100 series HPLC system (Agilent). Samples (8 μ l) were injected to a phenomenex Luna-NH2 2.1 \times 150 mm column at a flow rate of 200 μ l/min. The scan range was set as $m/z = 70$ –1100. The mobile phase was composed of A = water:acetonitrile 95:5 (v/v), ammonium acetate (20 mM), ammonium hydroxide (40 mM) and mobile phase B = 95% acetonitrile. Gradient was T0 = 0:100, T5 = 0:100, T45 = 100:0, and T60 = off with a 10 min re-equilibration time.

For the amino acid profile, an 1100 series HPLC system (Agilent) was coupled to a 6490 triple quadrupole mass spectrometer (Agilent), operated in multiple reaction monitoring

mode. The samples (10 μ l) were injected into an amino acid column 2.1 \times 100 mm (Imtakt) with a flow rate of 300 μ l/min. The mobile phase was composed of A = acetonitrile/tetrahydrofuran/25 mM ammonium formate/formic acid at 9:75:16:0.3 (v/v/v/v) and B = acetonitrile, ammonium formate (100 mM) at 20:80 (v/v). The gradient was T0 = 100:0, T12 = 100:0, T15 = 0:100, and T25 = off with a 5-min re-equilibration time.

Bioinformatics

The analyses of ASNS gene expression pattern presented here are in part based upon dataset downloaded from the TCGA Research Network (<http://cancergenome.nih.gov/>). It includes TCGA Pan-Cancer RNA-seq expression data (level 3 data using Illumina HiSeq platform from February 2015) [22], NKI breast cancer data (Affymetrix Human Genome HG U133A arrays) [23] and NCBI-GEO dataset GSE52604 (Agilent Whole Human Genome Microarray 4 \times 44K G4112F) [24]. TCGA cancer types having no more than 5 samples of normal tissues were excluded from the analysis. Log₂ transformed expression values were used for plotting and statistical analysis. Standard box plots were used to visualize the expression distribution and differences among different sample types. Statistical significance of the expression differences between groups was determined using Welch's *t* test. Differences in overall survival between "high" and "low" expression groups (defined by the optimal cut-point derived using log-rank score tests) [56] were compared by Kaplan-Meier curves using the *Survival* package in R software. Three different datasets were used for Distal metastasis-free survival (DMFS) analyses. The first dataset (GSE25066 [25]) recruited a neoadjuvant cohort of 508 HER2-negative breast cancer cases treated with chemotherapy pre-operatively and endocrine therapy if ER-positive. The second dataset (GSE17705 [26]) recruited 298 ER-positive breast cancer patients uniformly treated with tamoxifen for 5 y. The third dataset (GSE12276 [27]) collected 204 primary tumors from breast cancer patients with known distal site(s) of relapse. Clinical and expression data for survival analysis were downloaded from January 2016. Patients having both clinical information and expression data were included in this study. TCGA breast cancer and head and neck cancer datasets were used for Pearson correlation analysis. Pearson's *R*-squared and *p*-value were calculated using Graphpad Prism 7.

Statistical analysis

All results are given as the mean \pm S.D. of at least 3 independent experiments. The Student *t* test and one-way analysis of variance (ANOVA) were used to ascertain statistical significance. Statistical significance was set as $p < 0.05$, 2-tailed. The log-rank test for survival analysis was done using GraphPad Prism 7. The comparative and statistical analyses of metabolites were performed using the XCMS software package (<http://XCMSOnline.scripps.edu/>) and unpaired parametric *t* test (Welch's *t* test). Analysis of the untargeted metabolomics data was first done with MetaboAnalyst 3.0 web server (<http://www.metaboanalyst.ca> [57]) using unequal variance *t* test, followed by Mummichog program (version v1.0.9) with the following

parameters: p -value cutoff = 0.05, network model = *Mus musculus* BioCyc 17.0, analytical mode of mass spec = negative. Putative metabolites were then run through MetaboAnalyst 3.0 using a hypergeometric test for overrepresentation analysis and relative-betweenness centrality for pathway topology analysis based on the KEGG database (Release 82.1).

Acknowledgements

We thank members of Dr. Ann's laboratory for helpful discussions on the manuscript. We thank Drs. Craig D. Logsdon and Zobeida Cruz-Monserrate (UT MD Anderson Cancer Center) for the oncogenic KRAS mouse model. This work was supported in part by funds from the National Institutes of Health R01DE10742, R21DE023298 and R01DE026304 (to D.K.A.), R01DE023534 (to K.H.L. and D.K.A.) and P30CA033572 (supporting research work carried out in Core Facilities). We also thank Dr. Nancy Linford for editing.

Disclosure of potential conflicts of interest

The authors declare no competing financial interests.

References

- Yang S, Wang X, Contino G, et al. Pancreatic cancers require autophagy for tumor growth. *Genes Dev.* 2011 Apr 1;25(7):717–729. doi: 10.1101/gad.2016111gad.2016111 [pii]. PubMed PMID: 21406549; eng.
- Rosenfeldt MT, O'Prey J, Morton JP, et al. p53 status determines the role of autophagy in pancreatic tumour development. *Nature.* 2013 Dec 12;504(7479):296–300. doi: 10.1038/nature12865nature12865 [pii]. PubMed PMID: 24305049; eng.
- Yang A, Rajesh Kumar NV, Wang X, et al. Autophagy is critical for pancreatic tumor growth and progression in tumors with p53 alterations. *Cancer Discov.* 2014 Aug;4(8):905–913. doi: 10.1158/2159-8290.CD-14-0362 [doi] 2159–8290.CD-14-0362 [pii]. PubMed PMID: 24875860; PubMed Central PMCID: PMC4125497. eng.
- Wei H, Wei S, Gan B, et al. Suppression of autophagy by FIP200 deletion inhibits mammary tumorigenesis. *Genes Dev.* 2011 Jul 15;25(14):1510–1527. doi: 10.1101/gad.205101125/14/1510 [pii]. PubMed PMID: 21764854; eng.
- Eng CH, Wang Z, Tkach D, et al. Macroautophagy is dispensable for growth of KRAS mutant tumors and chloroquine efficacy. *Proc Natl Acad Sci USA.* 2016 Jan 5;113(1):182–187. doi: 10.1073/pnas.1515617113 1515617113 [pii]. PubMed PMID: 26677873; eng.
- Galluzzi L, Pietrocola F, Bravo-San Pedro JM, et al. Autophagy in malignant transformation and cancer progression. *EMBO J.* 2015 Apr 1;34(7):856–880. doi: 10.15252/embj.201490784 embj.201490784 [pii]. PubMed PMID: 25712477; eng.
- Guo JY, Xia B, White E. Autophagy-mediated tumor promotion. *Cell.* 2013 Dec 5;155(6):1216–1219. doi: 10.1016/j.cell.2013.11.019S0092-8674(13)01468-2 [pii]. PubMed PMID: 24315093; eng.
- Kenific CM, Debnath J. Cellular and metabolic functions for autophagy in cancer cells. *Trends Cell Biol.* 2015 Jan;25(1):37–45. doi: 10.1016/j.tcb.2014.09.001S0962-8924(14)00158-5 [pii]. PubMed PMID: 25278333; eng.
- Tsai C-H, Li C-H, Cheng Y-W, et al. The inhibition of lung cancer cell migration by AhR-regulated autophagy. *Sci Rep.* 2017 Feb 14;7:41927. doi: 10.1038/srep41927 [doi] srep41927 [pii]. PubMed PMID: 28195146; PubMed Central PMCID: PMC5307309. eng.
- Hu J, Meng Y, Zhang Z, et al. MARCH5 RNA promotes autophagy, migration, and invasion of ovarian cancer cells. *Autophagy.* 2017 Feb;13(2):333–344. doi: 10.1080/15548627.2016.1256520 [doi]. PubMed PMID: 27875077; PubMed Central PMCID: PMC45324849. eng.
- Fu Y, Cruz-Monserrate Z, Helen Lin H, et al. Ductal activation of oncogenic KRAS alone induces sarcomatoid phenotype. *Sci Rep.* 2015;5:13347. doi: 10.1038/srep13347srep13347 [pii]. PubMed PMID: 26289340; PubMed Central PMCID: PMC4642517. eng. PMID:26289340
- Hara T, Nakamura K, Matsui M, et al. Suppression of basal autophagy in neural cells causes neurodegenerative disease in mice. *Nature.* 2006 Jun 15;441(7095):885–889. doi: nature04724 [pii] 10.1038/nature04724. PubMed PMID: 16625204; eng.
- Lin HH, Lin S-M, Chung Y, et al. Dynamic involvement of ATG5 in cellular stress responses. *Cell Death Dis.* 2014;5:e1478. doi: 10.1038/cddis.2014.428 cddis2014428 [pii]. PubMed PMID: 25341032; eng. PMID:25341032
- Mizushima N, Komatsu M. Autophagy: renovation of cells and tissues. *Cell.* 2011 Nov 11;147(4):728–741. doi: 10.1016/j.cell.2011.10.026S0092-8674(11)01276-1 [pii]. PubMed PMID: 22078875; eng.
- Otera H, Wang C, Cleland MM, et al. Mff is an essential factor for mitochondrial recruitment of Drp1 during mitochondrial fission in mammalian cells. *J Cell Biol.* 2010 Dec 13;191(6):1141–1158. doi: 10.1083/jcb.201007152 [doi] jcb.201007152 [pii]. PubMed PMID: 21149567; PubMed Central PMCID: PMC3002033. eng.
- Zhang Z, Liu L, Wu S, et al. Drp1, Mff, Fis1, and MiD51 are coordinated to mediate mitochondrial fission during UV irradiation-induced apoptosis. *FASEB J.* 2016 Jan;30(1):466–476. doi: 10.1096/fj.15-274258 [doi] fj.15-274258 [pii]. PubMed PMID: 26432782; eng.
- Son J, Lyssiotis CA, Ying H, et al. Glutamine supports pancreatic cancer growth through a KRAS-regulated metabolic pathway. *Nature.* 2013 Apr 4;496(7443):101–105. doi: 10.1038/nature12040 nature12040 [pii]. PubMed PMID: 23535601; eng.
- Ying H, Kimmelman AC, Lyssiotis CA, et al. Oncogenic Kras maintains pancreatic tumors through regulation of anabolic glucose metabolism. *Cell.* 2012 Apr 27;149(3):656–670. doi: 10.1016/j.cell.2012.01.058S0092-8674(12)00352-2 [pii]. PubMed PMID: 22541435; eng.
- Mizushima N. Autophagy: process and function. *Genes Dev.* 2007 Nov 15;21(22):2861–2873. doi: 21/22/2861 [pii] 10.1101/gad.1599207 [doi]. PubMed PMID: 18006683; Eng.
- Kanehisa M, Goto S, Sato Y, et al. Data, information, knowledge and principle: back to metabolism in KEGG. *Nucleic Acids Res.* 2014 Jan;42(Database issue):D199–D205. doi: 10.1093/nar/gkt1076 [doi] gkt1076 [pii]. PubMed PMID: 24214961; PubMed Central PMCID: PMC3965122. eng.
- Zhang B, Dong L-W, Tan Y-X, et al. Asparagine synthetase is an independent predictor of surgical survival and a potential therapeutic target in hepatocellular carcinoma. *Brit J Cancer.* 2013 Jul 9;109(1):14–23. doi: 10.1038/bjc.2013.293. PubMed PMID: 23764751; PubMed Central PMCID: PMC3708586.
- The Cancer Genome Atlas Research Network, Weinstein JN, Collisson EA, Mills GB, et al. The Cancer Genome Atlas Pan-Cancer analysis project. *Nature Genet.* 2013 Oct;45(10):1113–1120. doi: 10.1038/ng.2764 [doi] ng.2764 [pii]. PubMed PMID: 24071849; PubMed Central PMCID: PMC3919969. eng.
- van Vliet MH, Reyal F, Horlings HM, et al. Pooling breast cancer datasets has a synergetic effect on classification performance and improves signature stability. *BMC Genom.* 2008 Aug 06;9:375. doi: 10.1186/1471-2164-9-375 [doi] 1471-2164-9-375 [pii]. PubMed PMID: 18684329; PubMed Central PMCID: PMC2527336. eng.
- Salhia B, Kiefer J, Ross JTD, et al. Integrated genomic and epigenomic analysis of breast cancer brain metastasis. *PLoS One.* 2014;9(1):e85448. doi: 10.1371/journal.pone.0085448 [doi] PONE-D-13-28131 [pii]. PubMed PMID: 24489661; PubMed Central PMCID: PMC3906004. eng. PMID:24489661
- Hatzis C. A genomic predictor of response and survival following taxane-anthracycline chemotherapy for invasive breast cancer. *JAMA.* 2011 May 11;305(18):1873–1881. doi: 10.1001/jama.2011.593 [doi] 305/18/1873 [pii]. PubMed PMID: 21558518; eng.
- Symmans WF, Hatzis C, Sotiriou C, et al. Genomic index of sensitivity to endocrine therapy for breast cancer. *J Clin Oncol: Off J Am Soc Clin Oncol.* 2010 Sep 20;28(27):4111–4119. doi: 10.1200/JCO.2010.28.4273 [doi]. PubMed PMID: 20697068; PubMed Central PMCID: PMC3965122. eng.
- Bos PD, Zhang XH-F, Nadal C, et al. Genes that mediate breast cancer metastasis to the brain. *Nature.* 2009 Jun 18;459(7249):1005–

1009. doi: 10.1038/nature08021 [doi] nature08021 [pii]. PubMed PMID: 19421193; PubMed Central PMCID: PMCPMC2698953. eng.
- [28] Amaravadi R, Kimmelman AC, White E. Recent insights into the function of autophagy in cancer. *Genes Dev.* **2016 Sep 01**;30(17):1913–1930. doi: 10.1101/gad.287524.116 [doi] 30/17/1913 [pii]. PubMed PMID: 27664235; PubMed Central PMCID: PMCPMC5066235. eng.
- [29] Liu J, Debnath J. The evolving, multifaceted roles of autophagy in cancer. *Adv Cancer Res.* **2016**;130:1–53. doi: 10.1016/bs.acr.2016.01.005 [doi] S0065-230X(16)30005-7 [pii]. PubMed PMID: 27037750; eng. PMID:27037750
- [30] Mishra P, Chan DC. Metabolic regulation of mitochondrial dynamics. *J Cell Biol.* **2016 Feb 15**;212(4):379–387. doi: 10.1083/jcb.201511036 [doi] jcb.201511036 [pii]. PubMed PMID: 26858267; PubMed Central PMCID: PMCPMC4754720. eng.
- [31] Kashatus JA, Nascimento A, Myers LJ, et al. Erk2 phosphorylation of Drp1 promotes mitochondrial fission and MAPK-driven tumor growth. *Mol Cell.* **2015 Feb 5**;57(3):537–551. doi: 10.1016/j.molcel.2015.01.002 S1097-2765(15)00003-9 [pii]. PubMed PMID: 25658205; eng.
- [32] Serasinghe MN, Wieder SY, Renault TT, et al. Mitochondrial division is requisite to RAS-induced transformation and targeted by oncogenic MAPK pathway inhibitors. *Mol Cell.* **2015 Feb 5**;57(3):521–536. doi: 10.1016/j.molcel.2015.01.003 S1097-2765(15)00004-0 [pii]. PubMed PMID: 25658204; eng.
- [33] Weinberg F, Hamanaka R, Wheaton WW, et al. Mitochondrial metabolism and ROS generation are essential for Kras-mediated tumorigenicity. *Proc Nat Acad Sci USA.* **2010 May 11**;107(19):8788–8793. doi: 10.1073/pnas.1003428107 1003428107 [pii]. PubMed PMID: 20421486; eng.
- [34] Ducommun S, Deak M, Sumpton D, et al. Motif affinity and mass spectrometry proteomic approach for the discovery of cellular AMPK targets: identification of mitochondrial fission factor as a new AMPK substrate. *Cell Signal.* **2015 May**;27(5):978–988. doi: 10.1016/j.cellsig.2015.02.008 [doi] S0898-6568(15)00042-X [pii]. PubMed PMID: 25683918; eng.
- [35] Toyama EQ, Herzig S, Courchet J, et al. Metabolism. AMP-activated protein kinase mediates mitochondrial fission in response to energy stress. *Science.* **2016 Jan 15**;351(6270):275–281. doi: 10.1126/science.aab4138 [doi] 351/6270/275 [pii]. PubMed PMID: 26816379; PubMed Central PMCID: PMCPMC4852862. eng.
- [36] Cheong H, Lu C, Lindsten T, et al. Therapeutic targets in cancer cell metabolism and autophagy. *Nat Biotechnol.* **2012 Jul**;30(7):671–678. doi: 10.1038/nbt.2285 nbt.2285 [pii]. PubMed PMID: 22781696; eng.
- [37] Shintani T. Autophagy in health and disease: a double-edged sword. *Science.* **2004 Nov 5**;306(5698):990–995. doi: 10.1126/science.1099993. PubMed PMID: 15528435; eng.
- [38] Mancias JD, Kimmelman AC. Targeting autophagy addiction in cancer. *Oncotarget.* **2011 Dec**;2(12):1302–1306. doi: 10.18632/oncotarget.384. PubMed PMID: 22185891; PubMed Central PMCID: PMCPMC3282086. eng.
- [39] White E. The role for autophagy in cancer. *J Clin Invest.* **2015 Jan**;125(1):42–46. doi: 10.1172/JCI73941. PubMed PMID: 25654549; PubMed Central PMCID: PMCPMC4382247.
- [40] Commisso C, Davidson SM, Soydaner-Azeloglu RG, et al. Macropinocytosis of protein is an amino acid supply route in Ras-transformed cells. *Nature.* **2013 May 30**;497(7451):633–637. doi: 10.1038/nature12138 nature12138 [pii]. PubMed PMID: 23665962; eng.
- [41] Kamphorst JJ, Nofal M, Commisso C, et al. Human pancreatic cancer tumors are nutrient poor and tumor cells actively scavenge extracellular protein. *Cancer Res.* **2015 Feb 1**;75(3):544–553. doi: 10.1158/0008-5472.CAN-14-2211 75/3/544 [pii]. PubMed PMID: 25644265; eng.
- [42] Seo J-W, Choi J, Lee S-Y, et al. Autophagy is required for PDAC glutamine metabolism. *Sci Rep.* **2016 Nov 28**;6:37594. doi: 10.1038/srep37594 [doi] srep37594 [pii]. PubMed PMID: 27892481; PubMed Central PMCID: PMCPMC5124864. eng.
- [43] Lin T-C, Chen Y-R, Kensicki E, et al. Autophagy: resetting glutamine-dependent metabolism and oxygen consumption. *Autophagy.* **2012 Oct**;8(10):1477–1493. doi: 10.4161/auto.21228 21228 [pii]. PubMed PMID: 22906967; eng.
- [44] Richards NGJ, Kilberg MS. Asparagine synthetase chemotherapy. *Annu Rev Biochem.* **2006**;75:629–654. doi: 10.1146/annurev.biochem.75.103004.142520. PubMed PMID: 16756505; eng.
- [45] Zhang J, Fan J, Venneti S, et al. Asparagine plays a critical role in regulating cellular adaptation to glutamine depletion. *Mol Cell.* **2014 Oct 23**;56(2):205–218. doi: 10.1016/j.molcel.2014.08.018 S1097-2765(14)00673-X [pii]. PubMed PMID: 25242145; eng.
- [46] Pan M, Reid MA, Lowman X, et al. Regional glutamine deficiency in tumours promotes dedifferentiation through inhibition of histone demethylation. *Nat Cell Biol.* **2016 Oct**;18(10):1090–1101. doi: 10.1038/ncb3410. PubMed PMID: 27617932.
- [47] Krall AS, Xu S, Graeber TG, et al. Asparagine promotes cancer cell proliferation through use as an amino acid exchange factor. *Nat Commun.* **2016**;7:11457. doi: 10.1038/ncomms11457 ncomms11457 [pii]. PubMed PMID: 27126896; eng. PMID:27126896
- [48] Ye J, Kumanova M, Hart LS, et al. The GCN2-ATF4 pathway is critical for tumour cell survival and proliferation in response to nutrient deprivation. *EMBO J.* **2010 Jun 16**;29(12):2082–2096. doi: 10.1038/emboj.2010.81 [doi] emboj201081 [pii]. PubMed PMID: 20473272; PubMed Central PMCID: PMCPMC2892366. eng.
- [49] Lorenzi PL, Llamas J, Gunsior M, et al. Asparagine synthetase is a predictive biomarker of L-asparaginase activity in ovarian cancer cell lines. *Mol Cancer Ther.* **2008 Oct**;7(10):3123–3128. doi: 10.1158/1535-7163.MCT-08-0589 [doi] 7/10/3123 [pii]. PubMed PMID: 18852115; PubMed Central PMCID: PMCPMC4123961. eng.
- [50] Hettmer S, Schinzel AC, Tchessalova D, et al. Functional genomic screening reveals asparagine dependence as a metabolic vulnerability in sarcoma. *Elife.* **2015**;4:e09436. doi: 10.7554/eLife.09436 e09436 [pii]. PubMed PMID: 26499495; eng. PMID:26499495
- [51] Lock R, Kenific CM, Leidal AM, et al. Autophagy-dependent production of secreted factors facilitates oncogenic RAS-driven invasion. *Cancer Discov.* **2014 Apr**;4(4):466–479. doi: 10.1158/2159-8290.CD-13-0841 2159-8290.CD-13-0841 [pii]. PubMed PMID: 24513958; eng.
- [52] Qu X, Sheng J, Shen L, et al. Autophagy inhibitor chloroquine increases sensitivity to cisplatin in QBC939 cholangiocarcinoma cells by mitochondrial ROS. *Plos One.* **2017 Mar 16**;12(3):e0173712. doi: ARTN e0173712 10.1371/journal.pone.0173712. PubMed PMID: WOS:000396318300065; English.
- [53] Warner KA, Adams A, Bernardi L, et al. Characterization of tumorigenic cell lines from the recurrence and lymph node metastasis of a human salivary mucoepidermoid carcinoma. *Oral Oncol.* **2013 Nov**;49(11):1059–1066. doi: 10.1016/j.oraloncology.2013.08.004. PubMed PMID: 24035723; PubMed Central PMCID: PMCPCM C3821871. eng.
- [54] Cheng C-T, Kuo C-Y, Ouyang C, et al. Metabolic stress-induced phosphorylation of KAP1 Ser473 blocks mitochondrial fusion in breast cancer cells. *Cancer Res.* **2016 Sep 1**;76(17):5006–5018. doi: 10.1158/0008-5472.CAN-15-2921 0008-5472.CAN-15-2921 [pii]. PubMed PMID: 27364555; eng.
- [55] Liang C-C, Park AY, Guan J-L. In vitro scratch assay: a convenient and inexpensive method for analysis of cell migration in vitro. *Nat Protoc.* **2007**;2(2):329–333. doi: nprot.2007.30 [pii] 10.1038/nprot.2007.30. PubMed PMID: 17406593; eng.
- [56] Mizuno H, Kitada K, Nakai K, et al. PrognScan: a new database for meta-analysis of the prognostic value of genes. *BMC Med Genom.* **2009 Apr 24**;2:18. doi: 10.1186/1755-8794-2-18 [doi] 1755-8794-2-18 [pii]. PubMed PMID: 19393097; PubMed Central PMCID: PMCPMC2689870. eng.
- [57] Xia J, Sinelnikov IV, Han B, et al. MetaboAnalyst 3.0—making metabolomics more meaningful. *Nucleic Acids Res.* **2015 Jul 01**;43(W1):W251–W257. doi: 10.1093/nar/gkv380 [doi] gkv380 [pii]. PubMed PMID: 25897128; PubMed Central PMCID: PMCPMC4489235. eng.
- [58] Gandre-Babbe S, van der Blik AM. The novel tail-anchored membrane protein Mff controls mitochondrial and peroxisomal fission in mammalian cells. *Mol Biol Cell.* **2008 Jun**;19(6):2402–2412. doi: 10.1091/mbc.E07-12-1287. PubMed PMID: WOS:000259155200006; English.